Aalborg Universitet

AALBORG UNIVERSITY
DENMARK

Multiple-Time-Scales Hierarchical Frequency Stability Control Strategy of Medium-Voltage Isolated Microgrid

Zhao, Zhuoli; Yang, Ping; Guerrero, Josep M.; Xu, Zhirong; C. Green, Timothy

Published in:
I E E E Transactions on Power Electronics

DOI (link to publication from Publisher):
10.1109/TPEL.2015.2496869

Publication date:
2016

Document Version
Early version, also known as pre-print

Link to publication from Aalborg University

Citation for published version (APA):
Zhao, Z., Yang, P., Guerrero, J. M., Xu, Z., & C. Green, T. (2016). Multiple-Time-Scales Hierarchical Frequency Stability Control Strategy of Medium-Voltage Isolated Microgrid. *I E E E Transactions on Power Electronics*, *31*(8), 5974 - 5991. https://doi.org/10.1109/TPEL.2015.2496869

General rights
Copyright and moral rights for the publications made accessible in the public portal are retained by the authors and/or other copyright owners and it is a condition of accessing publications that users recognise and abide by the legal requirements associated with these rights.

- Users may download and print one copy of any publication from the public portal for the purpose of private study or research.
- You may not further distribute the material or use it for any profit-making activity or commercial gain
- You may freely distribute the URL identifying the publication in the public portal -

Take down policy
If you believe that this document breaches copyright please contact us at vbn@aub.aau.dk providing details, and we will remove access to the work immediately and investigate your claim.

Multiple-Time-Scales Hierarchical Frequency Stability Control Strategy of Medium-Voltage Isolated Microgrid

Zhuoli Zhao, *Student Member, IEEE,* Ping Yang, *Member, IEEE,* Josep M. Guerrero, *Fellow, IEEE,* Zhirong Xu, *Student Member, IEEE, and* Timothy C. Green, *Senior Member, IEEE*

***Abstract*—In this paper, an islanded medium-voltage (MV) microgrid placed in Dongao Island is presented, which integrates renewable-energy-based distributed generations (DGs), energy storage system (ESS), and local loads. In an isolated microgrid without connection to the main grid to support the frequency, it is more complex to control and manage. Thus in order to maintain the frequency stability in multiple-time-scales, a hierarchical control strategy is proposed. The proposed control architecture divides the system frequency in three zones: (A) stable zone, (B) precautionary zone and (C) emergency zone. In this way, dynamic stability control that cope with disturbances in short-time scale is implemented by microgrid central controller (MGCC) within Zone B and Zone C. Meanwhile, steady-state stability control to solve the peaks and valleys problem of loads and DGs in long-time scale is executed by microgrid energy management system (MEMS) within Zone A. Furthermore, based on the developed complete small-signal state-space model, sensitivity analysis of the eigenvalues is conducted in order to reveal the dynamic stability margin of the MV microgrid, and to identify the proper range of the control parameters of Zone B. Theoretical analysis, time-domain simulation and field test results under various conditions and scenarios in the Dongao Island microgrid are presented to prove the validity of the introduced control strategy.**

***Index Terms*—Microgrid, frequency stability, multiple-time-scales, microgrid central controller (MGCC), microgrid energy management system (MEMS), stability analysis.**

I. Introduction

THE increasing penetration of renewable-energy-based distributed generations (DGs) in distribution networks promotes the emergence of new changes in power generation, transmission and distribution. Integrated DGs, energy storage systems (ESS), and local loads within a certain area, microgrid is an effective way to achieve active distribution networks, which can reduce the impact of large penetration of intermittent renewable energy integrated into the electrical grid, making the power system more reliable, safe, clean, and economical [1]–[3]. Microgrids combined with coordinated control, relaying protections, and intelligent dispatching systems, can operate in either grid-connected mode to exchange power with the main grid [4], or in islanded mode when applied in remote areas, islands or faults occur in the external power grid. Isolated microgrids, often named minigrids, are autonomous systems that can achieve self-control, protection and management [5], [6].

In recent years, many related technologies on islanded operation of microgrid have been developed, such as energy management [7]–[8], decentralized and hierarchical control [9]–[11], power quality compensation [12]–[13], and protection schemes [14]–[15], applied to laboratory systems or demonstration projects [16]–[20]. During islanded operation, without a fast and effective power balance strategy, frequency may present high fluctuations and instabilities due to the high penetration of intermittent renewable energy [21]. Power electronic converters based DGs play a significant role in maintaining the stability of microgrids, since they show faster transient response and higher controllability than conventional rotating machines interfaced DGs [22]–[24]. Normally, power electronic converters based DGs can be connected to the microgrid through three major kinds of interfaces: grid-forming, grid-feeding, and grid-supporting power converters [22], [25]. Grid-forming power converters are utilized as voltage source in the absent of master unit in a microgrid. Actually, most of the renewable-energy-based DGs are controlled in grid-feeding mode as current source, thus they cannot directly control the frequency and voltage in microgrid. On the other hand, grid supporting power converters can be controlled as voltage source or current source based on droop concept. Generally, the major purpose is to participate in the regulation of the frequency and voltage amplitude of the microgrid through controlling the active and reactive power injection or absorption.

Originally applied in line-interactive UPS systems, voltage-source-based grid supporting approach have been widely extended to parallel inverters control in inverter-based

This work was supported in part by the National High Technology Research and Development Program of China (863 Program-2014AA052001), Science and Technology Planning Project of Guangdong Province (2012B040303005), Science and Technology Planning Project of Nansha District, Guangdong Province (2013P005), and Science and Technology Project of China Southern Power Grid Electric Power Research Institute (SEPRI-K143003).

Zhuoli Zhao, Ping Yang, and Zhirong Xu are with the School of Electric Power, South China University of Technology, Guangzhou 510640, China (e-mail: zhuoliscut@gmail.com; eppyang@scut.edu.cn; 407849739@qq.com).

Josep M. Guerrero is with the Department of Energy Technology, Aalborg University, 9220 Aalborg, Denmark (e-mail: joz@et.aau.dk).

Timothy C. Green is with the Department of Electrical and Electronic Engineering, Imperial College London, London SW7 2AZ, U.K. (e-mail: t.green@imperial.ac.uk).

microgrid [4]. Frequency and voltage magnitude droop control architectures are proposed to stabilize the frequency and voltage of microgrids, and to achieve power sharing in a decentralized manner during islanded operation [6], [26], [27]. However, it is shown that frequency and voltage deviations are inevitable, and accurate reactive power sharing are challenged due to the impact of mismatched feeder impedance [28], [29]. Also, system stability and dynamic are highly affected by the selected droop gains [6]. Furthermore, to obtain accurate power-sharing performance with a high droop gain, the microgrid may experience oscillations and instabilities [30]–[32]. To solve the power control problems, secondary control has been recently addressed based on extra communication system [9], [33], [34]. However, the proposed methods exist fundamental conflict that the secondary voltage control can worsen the already poor sharing of reactive power, while enforcing reactive power sharing can result in poorer voltage profiles than with only primary control conversely [35]. Moreover, most of the microgrid control structures reported in the current literature are proposed for particular microgrids only formed by ideal parallel inverters, which neglect the dynamic of the primary sources, thus being inappropriate to integrate the diversity of DGs in a certain area.

Recently, a few coordinated methods have been proposed to support the frequency and voltage in a multi-source microgrid that includes renewable-energy-based DGs and ESS. In [36], an improved grid-forming control scheme is developed, which can keep the charging voltage of battery banks under control without physical communication. A coordinated control architecture for power management of islanded microgrids is proposed in [37] where the flexible power control of each DG unit can be achieved with seamless modes changes. However, experimental results in [36] and [37] show that the steady-state frequency deviates from the nominal value seriously. In [38], the novel grid-feeding control (GFC) scheme is presented in ESS. It can be also observed that this control method is only capable of dealing with the disturbance of wind-speed variations. Incorporating the current-source-based grid supporting control (GSC) approach, the control concept in [5] includes load-frequency primary control and secondary control, which mimics the frequency control method in interconnected power systems. Furthermore, [39] extends the primary and secondary control from frequency to voltage. In regards to dynamic stability control in short-time scale, the aforementioned control schemes are not sufficient to guarantee the microgrid frequency stability for large transients, such as sudden huge load demands or faults. In the case of multi-source microgrids, a damping method to mitigate the underlying oscillation due to the introduction of GSC approach is not reported in the current literature. On the other hand, the power reserve management is a vital task for microgrid operation in long-time scale. Optimizing microgrid operation using model predictive control approach is presented in [40]–[41] where operation constraints and time-varying request are satisfied. In [42]–[43], multiagent system for real-time operation of a microgrid is studied to maximize the power production of DGs while maintaining the stability. However, the existing control strategies greatly increase the complexity of microgrid energy management, and are only verified in simulation or laboratory test beds. Therefore, it is necessary to develop effective steady-state stability control approach in long-time scale with high applicability and reliability, where the operation modes and the power supply scheduling of microgrid can be optimized or regulated according to the availability of renewable resources, load conditions, and state of charge (SoC) of the ESS.

Motivated by the above-mentioned difficulties, this paper introduces a multiple-time-scales hierarchical frequency stability control architecture with the capability to operate stably and reliably at different conditions. The control architecture is implemented in the medium-voltage (MV) microgrid demonstration project of Dongao Island in China. By using the proposed control strategy, the system frequency is divided into three zones: (A) stable zone, (B) precautionary zone, and (C) emergency zone. The dynamic stability control for short-time scale is implemented by the microgrid central controller (MGCC) within Zone B and Zone C, while steady-state stability control for long-time scale is executed by the microgrid energy management system (MEMS) within Zone A. In order to analyze and ensure stability of the MV isolated microgrid system, a complete small-signal state-space model of the microgrid which containing diesel generator set (DGS), battery energy storage system (BESS), squirrel cage induction generator (SCIG) wind turbine (WT), network and loads is established. The developed state-space model is adopted to analyze the dynamic stability margin of the microgrid and to identify the proper range of key control parameters. Theoretical analysis, simulation and site experimental results are used to verify the effectiveness of the proposed control strategy.

This paper is organized as follows. Section II illustrates the system configuration and control structure of the isolated MV microgrid. Section III describes the proposed frequency stability control strategy. The detailed small-signal dynamic model of the MV microgrid and corresponding stability analysis are presented in Section IV. In Section V, simulation and experimental results in the Dongao Island microgrid are presented. Finally, conclusion is given in Section VI.

II. MV Isolated Microgrid System in Dongao Island

A. System Configuration

Fig. 1 shows the hierarchically controlled MV microgrid in Dongao Island. This microgrid includes four 10-kV busbars, i.e., BUS-1, BUS-2, BUS-3 and BUS-4, three DGSs, four SCIG WTs, one BESS, six distribution substations (DSs), and several load banks. Interconnection of these components is achieved through 10-kV MV lines. The BESS is connected to BUS-2 via a 380 V/10 kV step-up transformer, which is located geographically near to the point of common coupling (PCC) of the SCIG WTs and residential loads. Besides, the load is composed of six DSs (DS1–DS6: unconnected in this work for the sake of safety) and adjustable load banks. These 10-kV adjustable load banks consist of RLC (resistance, inductance,

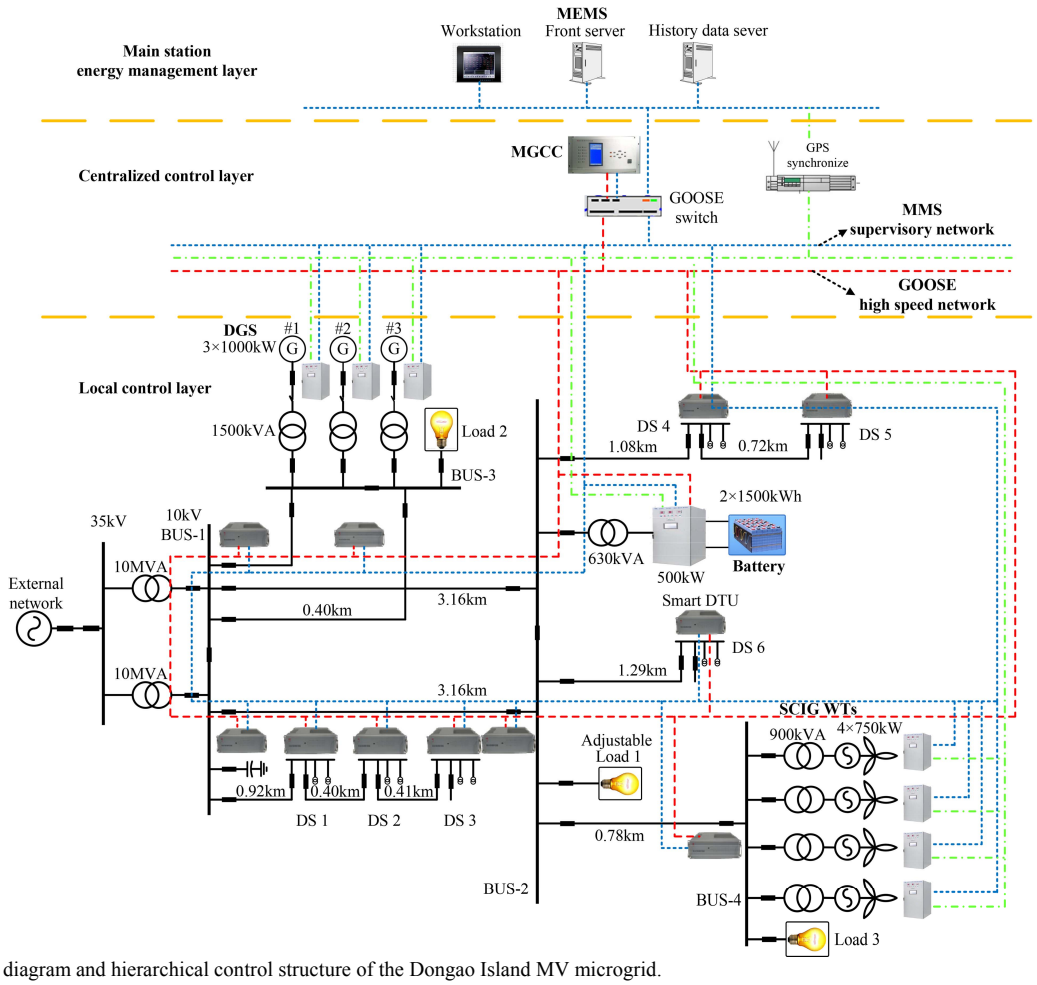

Fig. 1. Single-line diagram and hierarchical control structure of the Dongao Island MV microgrid.

and capacitor) branches, which are specially used in the field test and can be controlled automatically by remote signals. Details about the component parameters of the MV microgrid system are listed in Tables II and III.

B. Microgrid Control Architecture

Microgrid unified control system uses a hierarchical control structure, which comprises three control levels: (i) the local control layer, (ii) the centralized control layer, and (iii) the main station energy management layer, as presented in Fig. 1. The communication among the devices, the MGCC and the main station is performed by using the IEC61850 standard protocol. High-speed Ethernet data communication channel is implemented by using fiber optic ring network between the local control layer and the centralized control layer, which rapidly transmits the wide-area measurement sampled-value (SV) messaging, the device event data based on generic object-oriented substation event (GOOSE) network and the clock synchronization data based on the IEEE1588 standard. Thus, the data in these three networks achieved interconnectivity. Furthermore, Global Positioning System (GPS) devices provide a unified synchronization service for all apparatus in the different levels. Details of the three control levels are described as follows:

1) Local control layer is mainly composed of local intelligent terminals, i.e., smart distribution terminal unit (DTU), SCIG WT control system, DGS control system and BESS power conversion system. This layer automatically completes the wide-area data measurement, collection, and the operating conditions identification for the devices. The devices in the local control layer are required to provide two types of communication:

(a) High-speed GOOSE/SV for transmitting data between local control, protection units and MGCC. Moreover, the data must be transmitted with a 5-ms transmission interval.

(b) IEC61850 Manufacturing Message Service (MMS) layer for transmitting the steady-state data from field measurement and control devices to the main station, with a data refresh interval that cannot exceed two seconds.

2) Centralized control layer is responsible for the dynamic stability control, which is implemented by the MGCC.

3) Main station energy management layer is the top layer, equipped with MEMS that provides functionalities such as monitoring, comprehensive data acquisition and processing, steady-state stability control, and optimal dispatch.

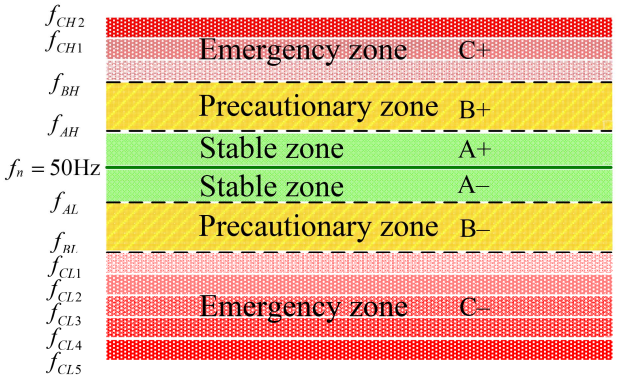

Fig. 2. Hierarchical frequency control strategy for the isolated microgrid.

III. Multiple-Time-Scales Hierarchical Frequency Stability Control Strategy Implementation

The objective of the frequency stability control strategy is to maintain the system frequency within the allowed range. Therefore, to mitigate frequency fluctuations due to the variations or switch on/off of distributed renewable resources and loads, additional control measures should be taken to remain the active power balance in the multiple-time-scales. Based on the frequency dynamic behaviors characteristic and the real-time values, the frequency stability control strategy of the microgrid system is divided into three zones, including stable zone, precautionary zone and emergency zone, which is referred in this paper as Zones A, B and C, respectively, as shown in Fig. 2. These proposed three zones reflect the level of frequency stability and are organized as follows.

1) Zone A: The frequency range in the frequency stable zone is $f_{AL} < f < f_{AH}$. Frequency deviation is minimal in this zone and frequency stable zone preventive control (FSZPC) is required to execute in long-time scale. Note that the allowable limit of the frequency deviation in interconnected grid is ±0.2 Hz in UCTE (Continental Europe) or ±0.1 Hz in North America [44]. The normal frequency fluctuation range of an isolated microgrid is greater than that of interconnected power systems since the capacity of a microgrid is comparatively small. Thus the allowable frequency deviation is set to ±0.3 Hz, which is less strict than in conventional power systems.

2) Zone B: The frequency range in the frequency precautionary zone is $f_{BL} < f \le f_{AL}$ & $f_{AH} \le f < f_{BH}$. When the frequency deviates from permissible frequency fluctuation range, frequency precautionary zone preventive control (FPZPC) that uses the buffering and regulating effect of the BESS has the responsibility to restore the frequency to Zone A. The selection of the border of Zone B (f_{BL}, f_{BH}) is discussed in Section V-A.

3) Zone C: The frequency range in the frequency emergency zone is $f_{CL} \le f \le f_{BL}$ & $f_{BH} \le f \le f_{CH}$ .When the frequency is deviated dramatically and is unavoidable to fall into Zone C, BESS is unable to restore the frequency back to Zone B effectively as the unbalanced power in the microgrid might have exceeded the charging/discharging limits of the BESS. Meanwhile, the DG units will trip off because of individual under/over-frequency protection. Therefore, in this case, frequency emergency zone preventive control (FEZPC) that results in sequential under-frequency load shedding (UFLS) and over-frequency generator tripping (OFGT) is supposed to restore the system frequency and protect the microgrid against a blackout.

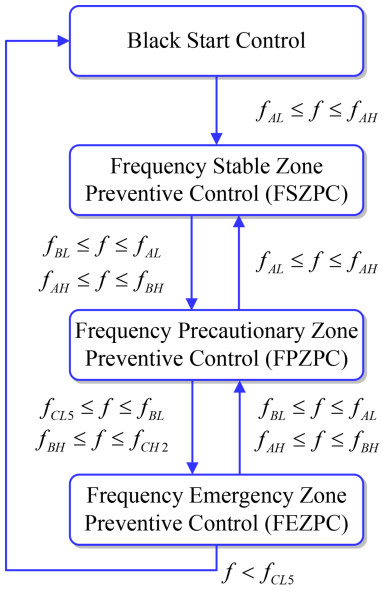

Fig. 3. Status switching flowchart for the hierarchical stability control strategy.

Consequently, frequency stability control strategy of isolated microgrid comprises the dynamic stability control and steady-state stability control based on different requirement of time scales. Dynamic stability control is composed of FPZPC in Zone B and FEZPC in Zone C, which is implemented by the MGCC within 65 ms through the high-speed GOOSE network. The MGCC is the last line of defense to ensure the safe and stable operation of the microgrid. On the other hand, steady-state stability control refers to the FSZPC in Zone A, which is executed by MEMS every 5 s through MMS supervisory network. It can be concluded that the hierarchical stability control strategy works in a status switching flowchart, as shown in Fig. 3.

A. *Frequency Stable Zone Preventive Control in MEMS*

When the microgrid is operating in isolated mode, it is essential to monitor for frequency of the system, generated power of the DG units, SoC of the BESS and the load condition in real time. If relevant variables exceed the limits, appropriate means of regulation must be implemented. For instance, regulation of dispatchable DG units, start-up/shutdown of DG units, interruption/ recovery of loads, and so forth. FSZPC in MEMS can solve the operation problem of frequency deviation in long-time scale caused by peaks and valleys of load consumption and wind power generation. The control objective of FSZPC is to maintain the microgrid system with sufficient spare capacity, which can guarantee the system to cope with large fluctuations in wind power and equipment failures. Meanwhile, the SCIG WTs power generation should be maximized. The flowchart representing the FSZPC in MEMS is depicted in Fig. 4.

Initially, the load rate of the DGS η is detected. When η is

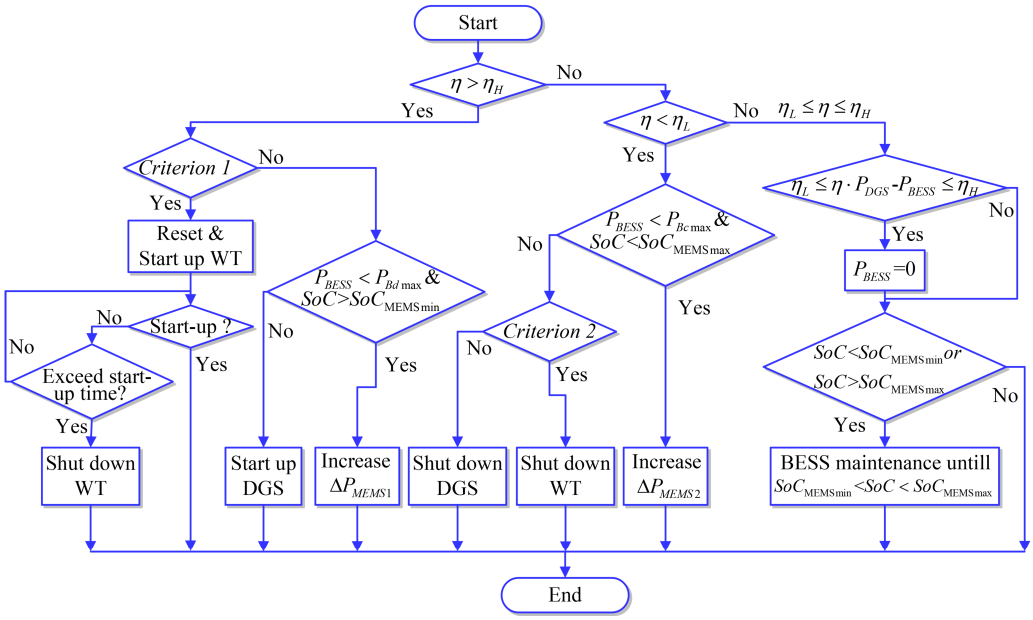

Fig. 4. FSZPC flowchart of MEMS.

higher than the load rate upper limit η_H , the program determines whether the condition is satisfied to turn on the WT first. If *Criterion 1* is satisfied, the command of WT start-up will be issued. Nevertheless, if the conditions are not met, the discharging conditions of BESS is checked: *"if P_{BESS} is less than discharging power limit $P_{Bd\max}$ and SoC is greater than $SoC_{MEMS\min}$, then the discharging power of BESS is increased; otherwise the DGS will be turned on afterwards"*. On the other hand, when η is below the load rate low limit η_L , the charging conditions of BESS is checked: *"if P_{BESS} is less than charging power limit $P_{Bc\max}$ and SoC is less than $SoC_{MEMS\max}$, then the charging power of BESS is raised; if the conditions are unsatisfied, then the DGS or WT will be shut down according to Criterion 2"*. Otherwise, when η is inside the limits ($\eta_L \le \eta \le \eta_H$), P_{BESS} will be restored to zero if $\eta_L \le \eta \cdot P_{DGS} - P_{BESS} \le \eta_H$ is satisfied. Then, the BESS performs maintenance program once SoC is out of the range of low/upper threshold for MEMS, i.e., $SoC_{MEMS\min}$ and $SoC_{MEMS\max}$. The detailed description of the commands and criteria in the flowchart are as follows:

1) BESS commands: The adjusting commands of the BESS are designed as follows:

$$\begin{aligned}\Delta P_{MEMS1} &= P_{DGS} - \Delta P_{aim\_up} \\ &= P_{DGS} - (P_{upper\_limit} - (P_{upper\_limit} - P_{low\_limit}) \times K_{osc})\end{aligned} \quad (1)$$

$$\begin{aligned}\Delta P_{MEMS2} &= P_{DGS} - \Delta P_{aim\_down} \\ &= P_{DGS} - (P_{low\_limit} + (P_{upper\_limit} - P_{low\_limit}) \times K_{osc})\end{aligned} \quad (2)$$

subjected to:

$$\textit{power constraints} \quad \Delta P_{MEMS1}, \Delta P_{MEMS2} < K_{reg} . P_{DGSrate} \quad (3)$$

$$\textit{sensitivity constraint} \quad P_{BESS} - P_{MEMS} > K_{sen} \quad (4)$$

where ΔP_{MEMS1} and ΔP_{MEMS2} are the commands corresponding with load rate exceeding η_H and η_L , P_{upper_limit} and P_{low_limit} are the upper limit and the low limit of the DGS output power, K_{osc} is the oscillation coefficient, K_{reg} is the regulating coefficient, P_{BESS} is the measured active power value of BESS, P_{MEMS} is the power command for the BESS and K_{sen} is the sensitivity coefficient, respectively. Note that the purpose of introducing the coefficient K_{osc} is to prevent the oscillation due to repetitively regulating BESS nearby the limits. Thus, the regulating objective is narrowed. Besides, ΔP_{MEMS} is restricted with power constraints; no repetitive instruction is issued if sensitivity constraint is not satisfied.

2) Criteria of start-up/shutdown of WTs: First, the penetration rate of wind power in the microgrid can be defined as follows:

$$S_{pr} = \frac{P_{WT\_T}}{P_{DGS\_T} + P_{WT\_T}} \quad (5)$$

where P_{DGS_T} and P_{WT_T} are the total capacity of the DGS and WTs in operation, respectively. Thus, the condition of starting up a WT (*Criterion 1*):

$$\begin{cases} \text{a) } \eta > \eta_H \\ \text{b) } S_{su} \le S_{pr1} \\ \text{c) } \Delta P_{sc} \ge k_{WT} \cdot P_{WTrate} \end{cases} \quad (6)$$

where S_{su} is the penetration rate after starting up a WT, ΔP_{sc} is the spare capacity of the DGS, k_{WT} is the impact coefficient of WT start-up, and P_{WTrate} is the rated power of the SCIG WT. Note that the regulating and impact resistance capability of the MV microgrid system improves with the increasing of the DGS in operation. Therefore, to upgrade the utilization rate of the WTs in the microgrid, η_H should be reduced reasonably based

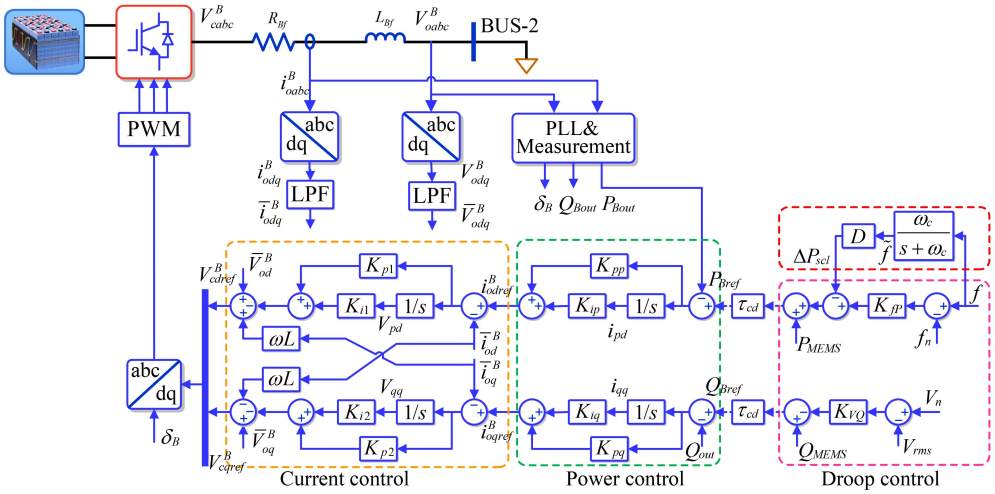

Fig. 5. FPZPC scheme.

on the quantity of DGS N. The condition of shutting down a WT (*Criterion 2*):

$$\begin{cases} \text{a)}\ \eta < \eta_L \\ \text{b)}\ S_{rt} > S_{pr2} \end{cases} \tag{7}$$

where S_{rt} is the real-time penetration rate.

B. Frequency Precautionary Zone Preventive Control in MGCC

When the system frequency is inside the precautionary zone, first, the shortage or the surplus of the active/reactive power in the microgrid system is calculated by the MGCC based on f/P and V/Q droop approaches [6], [39]. Then the power commands of the BESS are issued by MGCC through GOOSE channel with a communication delay τ_{cd}. The primary objective is to stabilize the system frequency fluctuations caused by the variations of the loads and renewable DGs in short-time scale. Note that by using centralized control schemes for BESS management can ensure the optimum operation of multi BESS easily when integrating more distributed BESS units into the MV microgrid, which is also the case for the future plans in Dongao pilot project. To be mentioned that the time delay of the high-speed GOOSE/SV network is usually considered to be in the order of 60 ms [45]. Therefore, the communication delay is normally negligible in such low-delay network [46]. Detailed analysis about the communication delay issue is given in Subsections IV-A-6 and IV-B-3.

Notice that, conventional droop control method has the inherent drawback that the dynamic performance of the system is weakened with low droop gains, while the stability margin is decreased with high droop gains [6]. Fig. 5 shows the proposed FPZPC scheme, which is based on the compensation and suppression of the frequency and power swings by introducing a supplementary control signal ΔP_{scl} to the active power generated by the f/P droop controller. It is worth mentioning that the supplementary control loop is inspired by the power system stabilizer (PSS) equipped in the synchronous machines for damping low frequency oscillation in interconnected power systems [47]. As can be seen from Fig. 5, frequency oscillation signal yielded from the derivative term of the frequency is used to inject a damping power signal ΔP_{scl} in the output of the f/P droop control loop. In this way, as additional control signal, ΔP_{scl} and ΔP are combined with the set-point command P_{MEMS} issued by MEMS in FSZPC scheme. Hence, the reference output power command of the BESS under the constraint of multiple-time scales can be expressed as:

$$P_{Bref} = P_{MEMS} + \overbrace{K_{fP}(f - f_n)}^{\Delta P} - \overbrace{K_{scl}.\frac{d\tilde{f}}{dt}}^{\Delta P_{scl}} \tag{8}$$

$$Q_{Bref} = Q_{MEMS} + \overbrace{K_{VQ}.(V_{rms} - V_n)}^{\Delta Q} \tag{9}$$

where K_{fP} is the frequency-active power droop gain, f is the monitored microgrid frequency, f_n is the reference frequency of the microgrid, K_{scl} is the coefficient of the supplementary control loop, K_{VQ} is the voltage-reactive power droop gain, V_{rms} is the rms value of the voltage of BUS-2, V_n is the reference voltage of BUS-2. $\tilde{f}$ can be obtained by a low-pass filter as follows:

$$\tilde{f} = \frac{\omega_c}{s + \omega_c} f \tag{10}$$

where ω_c is the filter cutoff frequency. On this basis, considering the constraints of maximum power limits of charging/discharging, if P_{Bref} exceeds the charging limit P_{Bcmax} or discharging limit P_{Bdmax}, then the reference power command is set to the limit values.

C. Frequency Emergency Zone Preventive Control in MGCC

If the frequency cannot be effectively controlled by the FPZPC scheme under large disturbances and falling into Zone C, UFLS or OFGT of MGCC is implemented to avoid frequency collapse.

1) UFLS: When the frequency of the microgrid decreases to

TABLE I
EXECUTION CONDITIONS OF UFLS

UFLS Stage	Frequency range	Delay time	Shedding load
1st stage	↓ 48.5–49.0Hz	$t \geq t_{uf1}$	DS6
2nd stage	↓ 48.0–48.5 Hz	$t \geq t_{uf2}$	DS5
3rd stage	↓ 47.7–48.0 Hz	$t \geq t_{uf3}$	DS4
4th stage	↓ 47.5–47.7 Hz	$t \geq t_{uf4}$	DS3
5th stage	↓ 45.0–47.5 Hz	$t \geq t_{uf5}$	DS2

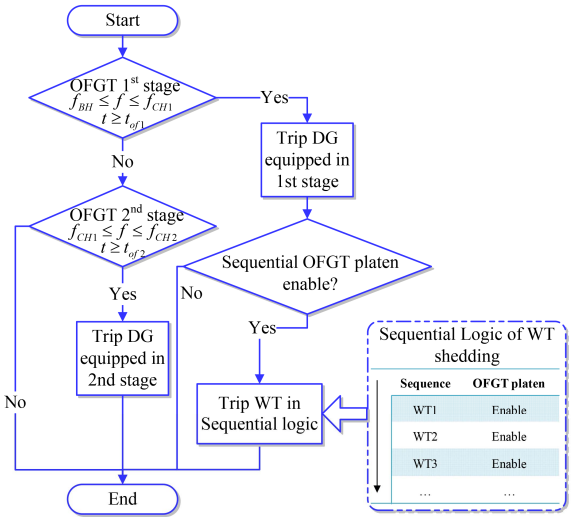

Fig. 6. Flowchart of OFGT.

$f_{CL} \leq f \leq f_{BL}$ region of Zone C, it is necessary to shed some of loads sequentially in accordance with the load levels. UFLS function in FEZPC has five basic stages, as presented in Table I.

2) OFGT: The flowchart of OFGT is illustrated in Fig. 6. It can be seen that when the frequency increases to $f_{BH} \leq f \leq f_{CH}$ region of Zone C, there are two stages of OFGT configured in FPZPC scheme. To guarantee the system stability under emergency conditions, uncontrollable microsources such as WTs should be disconnected in priority, and controllable microsources DGS may trip from the microgrid afterwards. Nevertheless, note that unreasonable OFGT scheme causes large impact on the frequency since the spare capacity is relatively low in a microgrid. Therefore, OFGT platen that can be used to enable/disable the tripping function of specific DG units is integrated into the sequential logic, which can be configured based on the field test results.

IV. MODELING AND STABILITY ANALYSIS OF THE MV ISOLATED MICROGRID SYSTEM

In order to analyze and ensure system stability, as well as to select the parameters of the FPZPC in Zone B properly, a small-signal state-space model of the MV microgrid is established and presented in Section IV-A. The systematic modeling approach can be readily extended to include more DG units and loads.

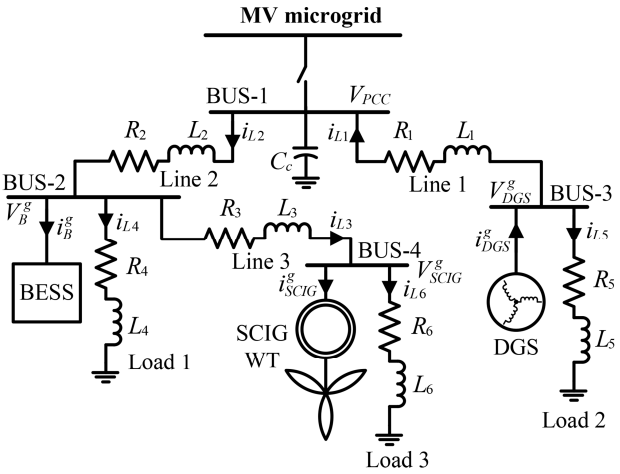

Fig. 7. Equivalent single-line diagram of the microgrid used for stability analysis.

A. Modeling of the MV Isolated Microgrid System

Fig. 7 shows the equivalent circuit of the microgrid system. The whole dynamic model consists of four major subsystems, i.e., BESS, DGS, SCIG WT and network including loads. Each subsystem is modeled based on its local reference frame. Since the microgrid includes more than one DG units, all interfaced state variables of the subsystems should be transformed to a global reference frame, based on the transformation defined in (11) [48]. The global reference frame of the microgrid (dq-frame) rotates at the angular frequency of ω_e, which is defined on the voltage vector of BUS-3. $d_D q_D$-frame, $d_B q_B$-frame and $d_I q_I$-frame are the local reference frame of DGS, BESS, SCIG WT locked to the rotor of DGS, BUS-2 and BUS-4, respectively; and the corresponding rotating speed is ω_D, ω_B and ω_I.

$$\begin{bmatrix} \Delta f_q^n \\ \Delta f_d^n \end{bmatrix} = \begin{bmatrix} \cos\delta_n^o & -\sin\delta_n^o \\ \sin\delta_n^o & \cos\delta_n^o \end{bmatrix} \begin{bmatrix} \Delta f_q^g \\ \Delta f_d^g \end{bmatrix} + \begin{bmatrix} -f_d^{no} \\ f_q^{no} \end{bmatrix} \Delta\delta_n \qquad (11)$$

In (11), $\delta_n (n = D, B, I)$ is the angle between the local reference frame of the nth subsystem and the global reference frame; $\begin{bmatrix} \Delta f_q^n & \Delta f_d^n \end{bmatrix}^T$ and $\begin{bmatrix} \Delta f_q^g & \Delta f_d^g \end{bmatrix}^T$ are the state variables in the aforementioned frames, respectively. Note that superscript "o" denotes the steady-state operating values in the equations of the following subsections.

1) Dynamic model of BESS

BESS unit is composed of a battery bank, bidirectional conversion system and power circuit, as shown in Fig. 5. The control system is composed of: 1) droop control loop, which is responsible for setting the values of active and reactive power to contribute to the regulation of the microgrid frequency and voltage; 2) power control loop to yield close control dynamic characteristics of the output power; and 3) inner current control loop, which has responsibility to control the current of the filter inductor and limit the inverter fault current.

As illustrated in Fig. 5, the power and current control are

achieved with conventional PI controllers (with gains K_{pp}, K_{ip}, K_{pq}, K_{iq}, K_{p1}, K_{i1}, K_{p2} and K_{i2}), including feed-forward terms. Therefore, the dynamic model of the power and current control loop can be derived as:

$$i^B_{odref} = K_{pp}(P_{Bref} - P_{Bout}) + K_{ip}\int (P_{Bref} - P_{Bout})dt \tag{12}$$

$$i^B_{oqref} = K_{pq}(Q_{Bref} - Q_{Bout}) + K_{iq}\int (Q_{Bref} - Q_{Bout})dt \tag{13}$$

$$V^B_{cdref} = -K_{p1}(i^B_{odref} - \bar{i}^B_{od}) - K_{i1}\int (i^B_{odref} - \bar{i}^B_{od})dt + \omega_B L_{Bf}\bar{i}^B_{oq} + \bar{V}^B_{od} \tag{14}$$

$$V^B_{cqref} = -K_{p2}(i^B_{oqref} - \bar{i}^B_{oq}) - K_{i2}\int (i^B_{oqref} - \bar{i}^B_{oq})dt - \omega_B L_{Bf}\bar{i}^B_{od} + \bar{V}^B_{oq} \tag{15}$$

where $\bar{i}^B_{od}$, $\bar{i}^B_{oq}$ are the filtered values of the current, $\bar{V}^B_{od}$ and $\bar{V}^B_{oq}$ are filtered voltage of BUS-2, i^B_{odref} and i^B_{oqref} are the reference values of the converter output current, V^B_{cdref} and V^B_{cqref} are the reference values of the converter output voltage. As seen from Fig. 5, the phase lock loop (PLL) is mainly used for microgrid synchronization. And the mathematical model of the PLL is given by

$$\omega_B = (\delta_{ref} - \delta_B)(K_{Bp} + \frac{K_{Bi}}{s}) \tag{16}$$

where K_{Bp} and K_{Bi} are the gains of the PI controller.

The power circuit consists of the equivalent resistor R_{Bf} and inductance L_{Bf}, which represents the lumped elements of the series filter and the interface transformer. The equations depicted the dynamic of the power circuit are written as

$$\frac{di^B_{od}}{dt} = -\frac{R_{Bf}}{L_{Bf}}i^B_{od} + \omega i^B_{oq} + \frac{1}{L_{Bf}}(V^B_{od} - V^B_{cd}) \tag{17}$$

$$\frac{di^B_{oq}}{dt} = -\frac{R_{Bf}}{L_{Bf}}i^B_{oq} - \omega i^B_{od} + \frac{1}{L_{Bf}}(V^B_{oq} - V^B_{cq}) \tag{18}$$

Thus, the state-space model of the BESS unit consists of the submodules of the control loop and power circuit, which can be established by linearizing the equations of (8)–(10) and (12)–(18). Furthermore, the model of the submodules transferred to the global reference frame using (11) can be derived as (19) and (20), respectively:

$$\Delta\dot{x}^g_{B,c} = A_{B,c}\Delta x^g_{B,c} + B_{B,c}\Delta x^g_{B,p} + B^u_{B,c}\Delta u_B + B^V_{B,c}\Delta V^g_B \tag{19}$$

$$\Delta\dot{x}^g_{B,p} = A_{B,p}\Delta x^g_{B,p} + B_{B,p}\Delta x^g_{B,c} + B^u_{B,p}\Delta u_B + B^V_{B,p}\Delta V^g_B + B^\omega_B\Delta\omega_B \tag{20}$$

In (19) and (20)

$$\Delta x^g_{B,c} = \left[\Delta\bar{V}^B_{oq} \quad \Delta\bar{V}^B_{od} \quad \Delta\bar{V}^B_{cq} \quad \Delta\bar{V}^B_{cd} \quad \Delta i_{qq} \quad \Delta i_{pd} \quad \Delta i^B_{oq} \quad \Delta i^B_{od} \quad \Delta V_{qq} \quad \Delta V_{pd} \quad \Delta\omega_B\right]^T,$$

$$\Delta x^g_{B,p} = \left[\Delta i^g_{oq} \quad \Delta i^g_{od}\right]^T,$$

$$\Delta u_B = \left[\Delta Q_{MEMS} \quad \Delta P_{MEMS} \quad \Delta V_n \quad \Delta\omega_n\right]^T,$$

$$\Delta V^g_B = \left[\Delta V^g_{oq} \quad \Delta V^g_{oq}\right]^T.$$

Note that Δi_{qq}, Δi_{pd}, ΔV_{qq} and ΔV_{pd} are the state variables represented the integrator states of the power and current controllers.

2) Dynamic model of DGS

DGS is composed of three blocks: (i) electrical system of the three-phase salient-pole synchronous generator; (ii) rotating mechanical system; (iii) governor and excitation systems. The mathematic model of the electrical system of DGS in the rotor reference frame $d_D q_D$ can be expressed as follows:

$$M\frac{d}{dt}(i^D) = Ni^D + v^D \tag{21}$$

where

$$i^D = \left[i^D_{Sqs} \quad i^D_{Sds} \quad i^D_{kq1} \quad i^D_{fd} \quad i^D_{kd}\right]^T,$$

$$v^D = \left[v^D_{Sqs} \quad v^D_{Sds} \quad v^D_{kq1} \quad e^D_{fd} \quad v^D_{kd}\right]^T$$

are the current and voltage vectors of the stator windings (Sqs, Sds), field winding (fd) and the damper windings ($kq1$, kd). The method of deriving matrices M and N is presented in [48].

The model of motion of the synchronous generator can be described by:

$$\frac{2H_S}{\omega_b}\frac{d\omega_{Dr}}{dt} + \frac{K_{DS}}{\omega_b}\frac{d\delta_D}{dt} = T_{mS} - T_{eS} \tag{22}$$

where H_S, K_{DS} are the inertia constant and damping factor, respectively. ω_{Dr} is the angular velocity of the rotor. T_{mS} and T_{eS} are the mechanical and electromagnetic torque, respectively, and

$$T_{eS} = -i^D_{Sds}(-i^D_{Sqs} + i^D_{kq1})X_{mq}i^D_{Sqs} + (-i^D_{Sds} + i^D_{kd} + i^D_{fd})X_{md} \tag{23}$$

where X_{mq} and X_{md} are the magnetizing reactance.

Please note that T_{mS} and e^D_{fd} are the output of the governor and excitation systems, respectively, and can be obtained from IEEE working group [49], [50]. A state-space model of DGS can be constructed by linearizing the equations of (21)–(23). Further, the model transferred to the global reference frame using (11) can be incorporated as follows:

$$\Delta\dot{x}^g_{DGS} = A_{DGS}\Delta x^g_{DGS} + B^u_{DGS}\Delta u_{DGS} + B^V_{DGS}\Delta V^g_{DGS} \tag{24}$$

where

$$\Delta x^g_{DGS} = \left[\Delta i^g_{Sqs} \quad \Delta i^g_{Sds} \quad \Delta i^D_{kq1} \quad \Delta i^D_{fd} \quad \Delta i^D_{kd} \quad \Delta\omega_{Dr} \quad \Delta\delta_D\right]^T,$$

$$\Delta u_{DGS} = \left[\Delta e^D_{fd} \quad \Delta T_{mS}\right]^T,\ \Delta V^g_{DGS} = \left[v^g_{Sqs} \quad v^g_{Sds}\right]^T.$$

3) Dynamic model of SCIG WT

The dynamic model of SCIG WT consists of: (i) the electrical system of the induction generator, (ii) the wind energy capturing mechanism, and (iii) the rotating shaft. The mathematical model of the induction generator in the local synchronously rotating reference frame $d_I q_I$ can be expressed by

$$W\frac{d}{dt}(i^I) = Yi^I + v^I \tag{25}$$

where

$$i^I = \left[i^I_{Wqs} \quad i^I_{Wds} \quad i^I_{Wqr} \quad i^I_{Wdr}\right]^T,\ v^I = \left[v^I_{Wqs} \quad v^I_{Wds} \quad v^I_{Wqr} \quad v^I_{Wdr}\right]^T$$

are the current and voltage vectors of the stator (Wqs, Wds), and the rotor (Wqr, Wdr), respectively. The matrices W and Y can be obtained from [48].

The electromagnetic torque of the SCIG can be written in terms of rotor and stator current as

$$T_{eI} = X_{MA}(i^I_{Wqs} i^I_{Wdr} - i^I_{Wds} i^I_{Wqr}) \tag{26}$$

where X_{MA} is the magnetizing reactance.

The shaft system of a SCIG WT unit can be represented by the two-mass model as follows:

$$\frac{2H_I}{\omega_b}\frac{d\omega_{Ir}}{dt} = K_{ss}\theta_{ss} - D_I\omega_{Ir} - T_{eI} \tag{27}$$

$$\frac{2H_{Tur}}{\omega_b}\frac{d\omega_W}{dt} = T_{mW} - K_{ss}\theta_{ss} - D_W\omega_W \tag{28}$$

$$\frac{d\theta_{ss}}{dt} = \omega_b(\omega_W - \omega_{Ir}) \tag{29}$$

where H_I, H_{Tur}, D_I and D_W are the inertia constant and damping factor of the induction generator rotor and wind turbine rotor, respectively. ω_{Ir} and ω_W are the mechanical angular velocity of the induction generator rotor and wind turbine rotor, respectively. K_{ss} is the shaft stiffness. T_{mW} is the input mechanical torque of the wind turbine. θ_{ss} is the shaft twist angle. The capturing mechanism of wind energy can be described by (30)–(31):

$$T_{mW} = \frac{\rho_A \pi C_W(\lambda,\beta) R_W^2 V_W^3}{2\omega_W} \tag{30}$$

$$\lambda = \frac{\omega_W}{V_W} R_W \tag{31}$$

where ρ_A is the air density, R_W is the blade length of wind turbine, V_W is the wind speed, λ is the tip-speed ratio, $C_W(\lambda,\beta)$ is the power coefficient, which is a function of λ and the pitch angle β [51].

Thus, using (25)–(31), the linearized state-space model of the SCIG WT in the global reference frame is derived as:

$$\Delta\dot{x}^g_{SCIG} = A_{SCIG}\Delta x^g_{SCIG} + B^u_{SCIG}\Delta u_{SCIG} + B^V_{SCIG}\Delta V^g_{SCIG} \tag{32}$$

where

$$\Delta x^g_{SCIG} = \begin{bmatrix}\Delta i^g_{Wqs} & \Delta i^g_{Wds} & \Delta i^I_{Wqr} & \Delta i^I_{Wdr} & \Delta\omega_{Ir} & \Delta\omega_W & \Delta\theta_{ss}\end{bmatrix}^T,$$

$$\Delta u_{SCIG} = \begin{bmatrix}\Delta v^I_{Wqr} & \Delta v^I_{Wdr} & \Delta T_{mW}\end{bmatrix}^T,\ \Delta V^g_{SCIG} = \begin{bmatrix}\Delta v^g_{Wqs} & \Delta v^g_{Wds}\end{bmatrix}^T.$$

4) Dynamic model of network including loads

As presented in Fig. 7, the dynamic of the network can be modeled in the form of the relationships between current and voltage as

$$V^g_{DGS} - V_{PCC} = R_1 i_{L1} + L_1\dot{i}_{L1} \tag{33}$$

$$V_{PCC} - V^g_B = R_2 i_{L2} + L_2\dot{i}_{L2} \tag{34}$$

$$V^g_B - V^g_{SCIG} = R_3 i_{L3} + L_3\dot{i}_{L3} \tag{35}$$

$$C_c\dot{V}_{PCC} = i_{L1} - i_{L2} \tag{36}$$

where R_n and $L_n (n = 1,2,3)$ are equivalent impedance of the series RL branches. i_{Ln} are the corresponding current vectors.

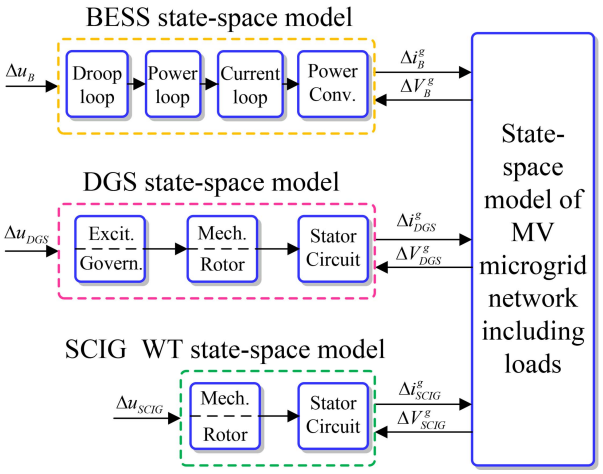

Fig. 8. Block diagram of the complete dynamic model of the MV microgrid.

V_{PCC} is the instantaneous voltage of BUS-1. C_c is the shunt-capacitor for reactive power compensation. Based on (33)–(36), the dynamic model of the microgrid network can be incorporated as follows:

$$\Delta\dot{x}^g_{NET} = A_{NET}\Delta x^g_{NET} + B^{V1}_{NET}\Delta V^g_{DGS} + B^{V2}_{NET}\Delta V^g_B + B^{V3}_{NET}\Delta V^g_{SCIG} \tag{37}$$

where $\Delta x^g_{NET} = \begin{bmatrix}\Delta i^{L1}_{qd} & \Delta i^{L2}_{qd} & \Delta i^{L3}_{qd} & \Delta V^{PCC}_{qd}\end{bmatrix}^T$. In addition, the voltage vectors of BUS-3, BUS-2 and BUS-4 can be obtained by

$$V^g_{DGS} = R_5(i^g_{DGS} - i_{L1}) + L_5\frac{d(i^g_{DGS} - i_{L1})}{dt} \tag{38}$$

$$V^g_B = R_4(i_{L2} - i^g_B - i_{L3}) + L_4\frac{d(i_{L2} - i^g_B - i_{L3})}{dt} \tag{39}$$

$$V^g_{SCIG} = R_6(i_{L3} - i^g_{SCIG}) + L_6\frac{d(i_{L3} - i^g_{SCIG})}{dt} \tag{40}$$

where R_n and $L_n (n = 4,5,6)$ are equivalent impedance of the adjustable load banks. Thus, the linearized equations of the voltage vectors can be written as

$$\Delta V^g_{DGS} = D^{11}_{NET}\Delta x^g_{NET} + D^{12}_{NET}\Delta\dot{x}^g_{NET} + E^{11}_{NET}\Delta x^g_{DGS} + E^{12}_{NET}\Delta\dot{x}^g_{DGS} \tag{41}$$

$$\Delta V^g_B = D^{21}_{NET}\Delta x^g_{NET} + D^{22}_{NET}\Delta\dot{x}^g_{NET} + E^{21}_{NET}\Delta x^g_{B,p} + E^{22}_{NET}\Delta\dot{x}^g_{B,p} \tag{42}$$

$$\Delta V^g_{SCIG} = D^{31}_{NET}\Delta x^g_{NET} + D^{32}_{NET}\Delta\dot{x}^g_{NET} + E^{31}_{NET}\Delta x^g_{SCIG} + E^{32}_{NET}\Delta\dot{x}^g_{SCIG} \tag{43}$$

5) Complete dynamic model of MV microgrid with negligible communication delay

Fig. 8 depicts the block representation for establishing the small-signal dynamic model of the MV microgrid with all of the subsystems integrated together. It is worth mentioning that the output current of the DG units Δi^g_{DGS}, Δi^g_B and Δi^g_{SCIG}, are the input signals of the microgrid network model, while the bus voltages vectors ΔV^g_{DGS}, ΔV^g_B and ΔV^g_{SCIG}, which can be eliminated using (41)–(43), can be treated as the output of the network and inputs of the DG units. Now, the complete state-space model of the MV autonomous microgrid can be constructed based on (19), (20), (24), (32) and (37):

$$\Delta\dot{x}_{MVMG} = A_{MVMG}\Delta x_{MVMG} + B_{MVMG}\Delta u_{MVMG} \tag{44}$$

where $\Delta x_{MVMG} = [\Delta x^g_{DGS} \quad \Delta x^g_{B,p} \quad \Delta x^g_{B,c} \quad \Delta x^g_{SCIG} \quad \Delta x^g_{NET}]^T$,

$\Delta u_{MVMG} = [\Delta u_{DGS} \quad \Delta u_B \quad \Delta u_{SCIG}]^T$.

6) Microgrid dynamic model considering communication delay

In order to carry out the delay-dependent stability analysis of the proposed FPZPC scheme of Zone B in Subsection IV-B-3 and show its robustness in the presence of communication delay, the state-space model of (44) is extended to consider a communication delay time τ_{cd} for the data transmission between MGCC and BESS, as depicted in Fig. 5. In this case, the equations of (8)–(9) should be modified as

$$P_{Bref} = P_{MEMS} + K_{fP}(f(t-\tau_{cd}) - f_n) - K_{scl}.\frac{d\tilde{f}(t-\tau_{cd})}{dt} \quad (45)$$

$$Q_{Bref} = Q_{MEMS} + K_{VQ}.(V_{rms}(t-\tau_{cd}) - V_n) \quad (46)$$

Therefore, the state-space model of the microgrid system based on delay differential equations (DDEs) can be given by

$$\Delta\dot{x}_{MVMG}(t) = A_{MVMG-NCD}\Delta x_{MVMG}(t) + A_{MVMG-CD}\Delta x_{MVMG}(t-\tau_{cd}) + B_{MVMG}\Delta u_{MVMG}(t) \quad (47)$$

Note that the matrices $A_{MVMG-NCD}$ and $A_{MVMG-CD}$ can be readily obtained based on the decomposed model in the previous subsections.

B. Design and Stability Analysis of the MV Isolated Microgrid System

The complete linearized state-space model of (44) is then to be adopted for conducting sensitivity analysis of eigenvalues in order to have a better evaluation of the proposed supplementary control loop in Fig. 5, and to design the critical control parameters of the FPZPC in Zone B in a way that both system stability margin and dynamic performance constraints are met. The key parameters of the microgrid system are selected to be the same as in the simulation, as provided in Tables II and III. And the detailed parameters of the DGS and SCIG WT can be found in [52] and [53], respectively. It is to be noted that since the focus of this paper is on frequency stability control method in MV microgrid, the voltage-reactive power droop gain K_{VQ} in FPZPC is remained constant throughout this work.

1) Sensitivity to control parameters

Sensitivity of the system eigenvalues to variations in the f/P droop gain K_{fP}, supplementary control loop gain K_{scl}, and the corresponding filter cutoff frequency ω_c, of the FPZPC in Zone B are demonstrated. Fig. 9 shows the trace of the microgrid dominant modes for the frequency droop gain K_{fP} variations in the range of –0.2 to –900 kW/Hz when the conventional f/P frequency control scheme in [6] and [39] is adopted in FPZPC. Note that the low-frequency oscillatory modes are identified to be the dominant modes of the system, which is essential for the stability analysis. Moreover, it can be seen that the dynamic characteristics of the MV microgrid are noticeably affected by three pairs of eigenvalues, i.e., (1, 2), (3, 4) and (5, 6). It is observed that eigenvalues (1, 2) is identified

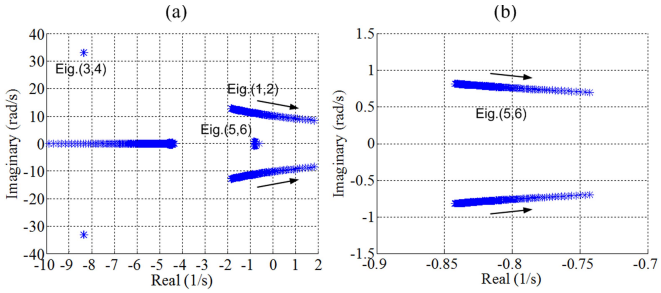

Fig. 9. (a) Trace of the dominant modes as a function of frequency droop gain ($-0.2\text{kW/Hz} \le K_{fP} \le -900\text{kW/Hz}$) with the conventional frequency control scheme reported in [6] and [39]. (b) Magnified trace of eigenvalues (5, 6).

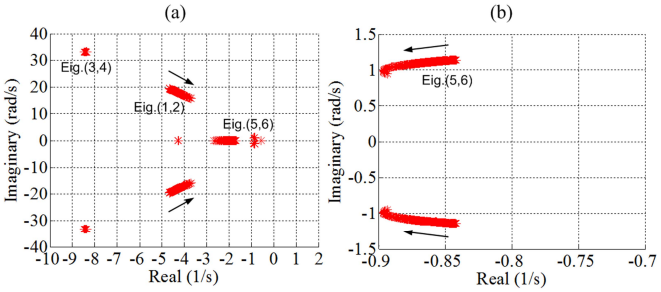

Fig. 10. (a) Trace of the dominant modes as a function of frequency droop gain ($-0.2\text{kW/Hz} \le K_{fP} \le -900\text{kW/Hz}$) with the proposed supplementary control loop in FPZPC ($K_{scl} = 0.3\,\text{kW.s}^2$). (b) Magnified trace of eigenvalues (5, 6).

to be the electromechanical mode of the microgrid system. As can be seen, the trace of the eigenvalues (1, 2) indicates that the f/P droop gain have remarkable impact on the electromechanical mode. It should be mentioned that high f/P droop gain can enhance the transient response of the microgrid. However, it can be seen from Fig. 9 that as the coefficient of f/P droop loop increases, the dominant mode (1, 2) shifts towards to the unstable region, which leads to more oscillatory or even instability of the microgrid.

Fig. 10 compares the system dominant eigenvalues spectrum when the supplementary control loop is introduced in the f/P conventional frequency control loop in FPZPC. It is shown that the dominant oscillatory modes of the system shift to the left-hand plane (LHP), which yields less oscillatory behavior. Moreover, the electromechanical mode shows less sensitive to the f/P droop gain compared with the conventional droop approach. This indicates that the microgrid system remains stable for a wider range of f/P droop gain variations. It is worth mentioning that using a high droop gain with larger stability margin is favorable during the operation of the MV microgrid.

Fig. 11 illustrates the loci of the dominant modes for the supplementary control loop gain K_{scl} variations in the range of 0 to 20 kW.s^2. Fig. 11 shows that as K_{scl} increases, the damping of the electromechanical mode represented by the eigenvalues (1, 2) goes up significantly. However, the loci of the eigenvalues (3, 4) and (5, 6) indicates the damping of the corresponding oscillatory modes first increase and then

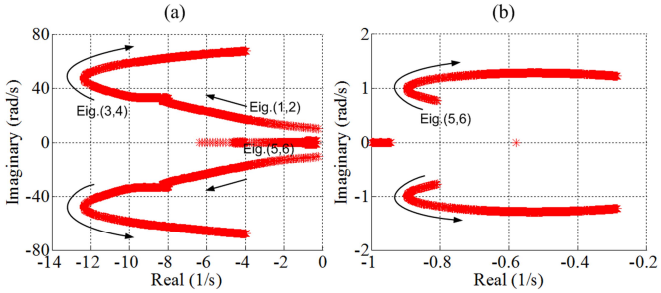

Fig. 11. (a) Trace of the dominant modes when K_{scl} is increased from 0 to 20 kW.s^2 ($K_{fP} = -400$ kW/Hz). (b) Magnified trace of eigenvalues (5, 6).

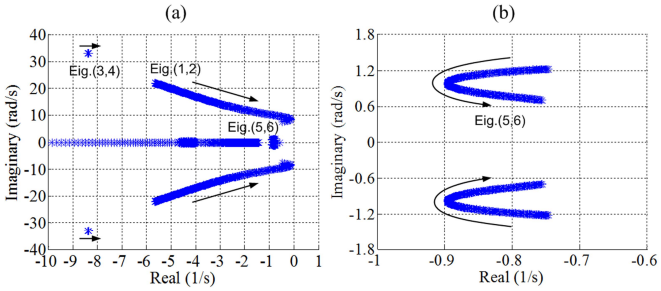

Fig. 12. (a) Trace of the dominant modes when ω_c is decreased from 50π to π rad/s ($K_{fP} = -400\text{kW/Hz}$, $K_{scl} = 0.3\,\text{kW.s}^2$). (b) Magnified trace of eigenvalues (5, 6).

decrease. It can be revealed that the damping ratio (ζ) of the eigenvalues (3, 4) reduces to 0.058 when K_{scl} increases to 20 kW.s^2, which might well become underlying factor leading instability of the microgrid. Therefore, K_{scl} should be limited according to the locations of the eigenvalues (3, 4) and (5, 6). As can be seen from Figs. 10 and 11, system stability margin is met even with high K_{fP} or K_{scl}. Hence, final values will be discussed and selected thoroughly in Section V-A considering charging/discharging limits of the BESS.

Fig. 12 shows the effect of the filter bandwidth on the dominant modes. It shows that as ω_c decreases from 50π to π rad/s, the damping of eigenvalues (5, 6) increases first, then decreases, whereas the damping of eigenvalues (1, 2) decreases significantly. Obviously, by selecting a high cutoff frequency of the frequency filter, the system stability margin can be increased. However, the attenuation property of the high frequency components is reduced, thus the noise will be amplified by the supplementary control loop and leads to output power oscillations of the BESS. On the contrary, a low cutoff frequency will impose a certain delay that can degrade the performance of the supplementary control loop and worsen the system stability. In this instance, the final value of $\omega_c = 20\pi$ rad/s was chosen to obtain the desirable transient response specifications, considering the tradeoff between high frequency noise attenuation and the response speed of the supplementary control loop.

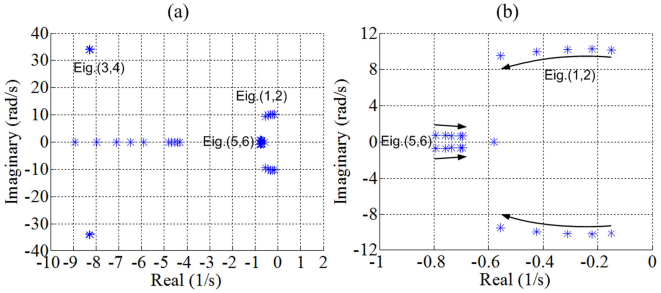

Fig. 13. (a) Trace of the dominant modes when the total load power in microgrid is increased from 800 kW to 1200 kW with the conventional frequency control scheme ($K_{fP} = -400\text{kW/Hz}$) reported in [6] and [39]. (b) Magnified trace of eigenvalues (1, 2) and (5, 6).

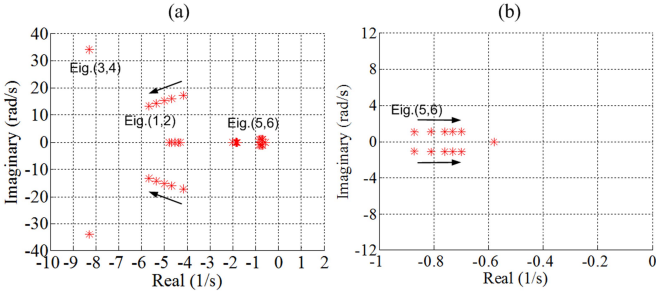

Fig. 14. (a) Trace of the dominant modes when the total load power in microgrid is increased from 800 kW to 1200 kW with the proposed FPZPC scheme ($K_{fP} = -400\text{kW/Hz}$, $K_{scl} = 0.3\,\text{kW.s}^2$). (b) Magnified trace of eigenvalues (5, 6).

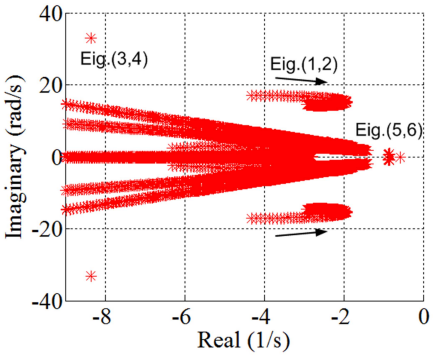

Fig. 15. System eigenvalues spectrum as the communication delays ranges from 0 to 500 ms.

2) Sensitivity to operating points

Figs. 13 and 14 show the trajectory of the dominant oscillatory modes as the total load (TL) power increases from 800 kW to 1200 kW, corresponding to conventional frequency control scheme and proposed supplementary control scheme in FPZPC, respectively. As shown in Figs. 13 and 14, with the total load in the microgrid grows, the damping of the electromechanical mode increases, while the mode represented by eigenvalues (5, 6) is attracted to the unstable region. Comparing Fig. 14 to Fig. 13, obviously eigenvalues (1, 2) and (5, 6) shift to the LHP when adopting the supplementary control loop. This behavior clearly reveals that the proposed supplementary control loop is effective for stability margin enhancement in different load power conditions.

TABLE II
SYSTEM PARAMETERS

Elements	Types	Value
BESS	Power converter	500 kW
DGS	Synchronous generator	1000 kW
SCIG WT	Asynchronous generator	750 kW
Line 1	Series RL branch	$0.180 + j0.147\ (\Omega)$
Line 2	Series RL branch	$1.422 + j1.163\ (\Omega)$
Line 3	Series RL branch	$0.351 + j0.287(\Omega)$
Load 1 (Adjustable load banks)	Series RL load	2000 kW / 1000 kVar
Load 2	Series RL load	100 kW / 50 kVAr
Load 3	Series RL load	50 kW / 50 kVAr
Capacitor C_c	Fix-capacitor bank	250 kVAr

TABLE III
MAIN BESS PARAMETERS

Parameter		Symbol	Value
DC link voltage		V_{dc}	500 V-835 V
PWM switching frequency		f_s	4 kHz
Equivalent impedance		L_{Bf}; R_{Bf}	L:1.15mH; R:0.002Ω
Power controller	Proportional gains	K_{pp}; K_{pq}	10
	Integral gains	K_{ip}; K_{iq}	40
Current controller	Proportional gains	K_{p1}; K_{p2}	12
	Integral gains	K_{i1}; K_{i2}	260
PLL	Proportional gains	K_{Bp}	180
	Integral gains	K_{Bi}	3200

3) Impact of communication delay

One of the major challenges facing the proposed FPZPC in Zone B is the effect of communication delay. To evaluate the impact of the communication delay on the microgrid stability, Chebyshev's discretization based method proposed in [54] is adopted to calculate the eigenvalues of the system with DDEs represented by (47). Fig. 15 demonstrates the system eigenvalues spectrum as the communication delays ranges from 0 to 500 ms. Note that $M = 3$ is chosen for the numbers of nodes formatting the Chebyshev's discretization scheme. As can be seen, the dominant eigenvalues of the microgrid system keep in the LHP, which indicates that the introduced frequency control strategy remains stable even though the communication delay is assumed to be as large as 500 ms. Therefore, system stability will not be compromised with the proposed centralized control structure for BESS management.

V. VERIFICATION RESULTS AND DISCUSSION

In order to verify the proposed multiple-time-scales hierarchical frequency stability control strategy, comprehensive simulations analysis under MATLAB/Simulink environment and experimental study in Dongao Island microgid have been conducted. The main parameters of the microgrid system are selected to be the same in both simulation and experiments, as listed in Tables II and III.

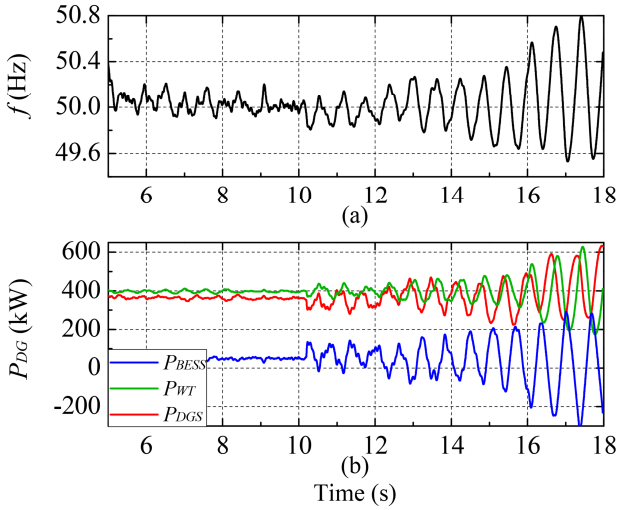

Fig. 16. Responses of the MV microgrid as K_{fP} is increased from –80 to –720 kW/Hz with the conventional f/P frequency control scheme reported in [6] and [39]. (a) Frequency. (b) Active power: BESS (P_{BESS}), SCIG WT (P_{WT}), and DGS (P_{DGS}).

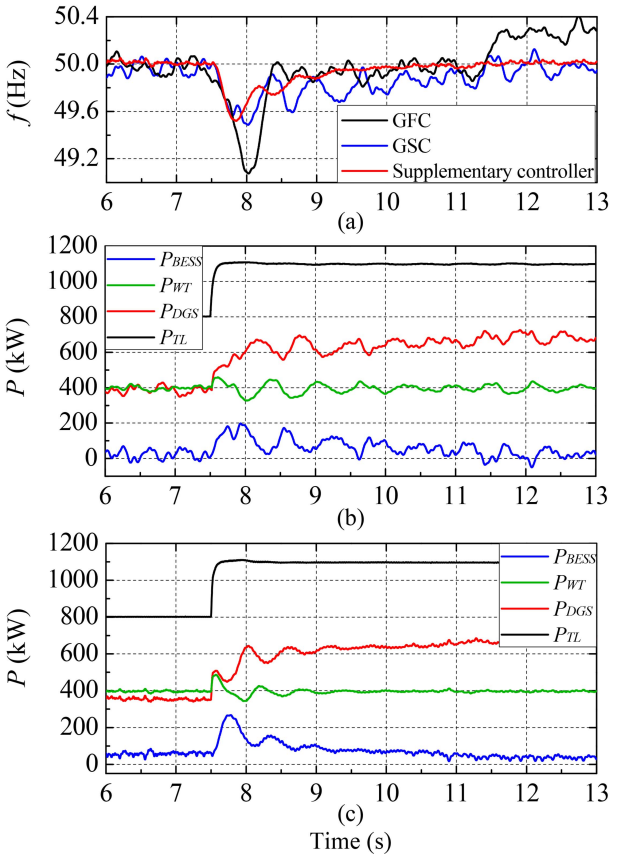

Fig. 17. Responses of the MV microgrid under step load increase of 300kW with different control schemes. (a) Comparison of frequency responses with GFC reported in [38], conventional GSC reported in [6] and [39] ($K_{fP} = -400$kW/Hz), and the proposed control scheme in FPZPC ($K_{scl} = 0.3\,\text{kW}.\text{s}^2$). (b) Active power response with conventional GSC: BESS (P_{BESS}), SCIG WT (P_{WT}), DGS (P_{DGS}) and the total load in microgrid (P_{TL}). (c) Active power response with the proposed control scheme.

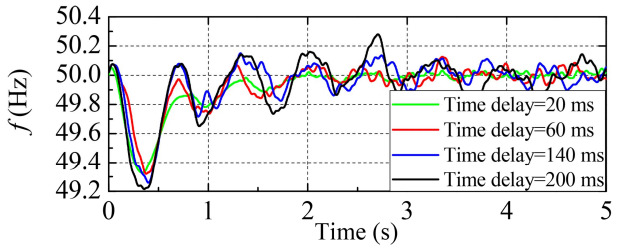

Fig. 18. Frequency response at different time delays.

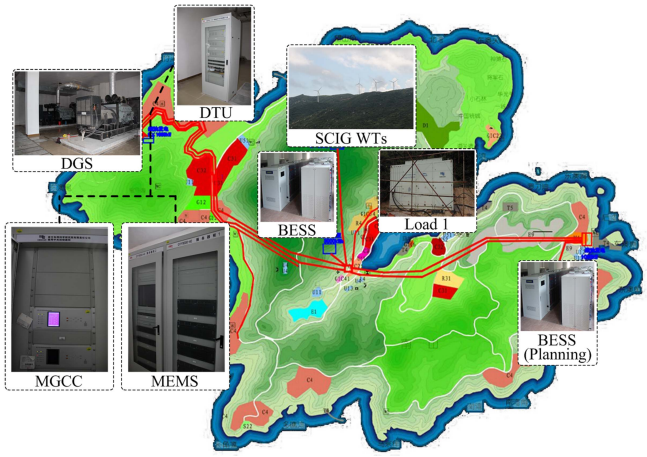

Fig. 19. Main primary equipment and secondary equipment in Dongao Island microgrid.

A. *Evaluation of FPZPC in MGCC*

Comprehensive simulated results have been obtained to examine the performance of the introduced control scheme of FPZPC in Zone B.

Fig. 16 shows the dynamic responses of the system under a step change of frequency droop gain K_{fP} from –80 to –720 kW/Hz at $t = 10.2$ s with the conventional f/P frequency control scheme reported in [6] and [39]. It can be seen that the introduction of droop controller in a MV multi-source microgrid would introduce oscillations in system frequency and active power of the microsources, which reveals the intrinsic nature of the conventional droop control approach. Moreover, Fig. 16 suggests that as K_{fP} is increased, the system appears much more oscillatory performance, and eventually instability can be yielded. Note that this agrees with the findings from the sensitivity analysis presented in Section IV-B.

Fig. 17 shows the performance of the microgrid under different control schemes when a step load increase of 300 kW occurs at $t = 7.5$ s. Compared with the responses of GFC reported in [38], as can be seen from Fig. 17(a), frequency drop and fluctuations subsequent to a step load increase can be mitigated and stabilized significantly when adopting the droop control approach. Additionally, comparing the responses of the proposed control scheme, as shown in Fig. 17(a) and (c), to the conventional GSC (see Fig. 17(a) and (b)) clearly verifies the effectiveness of the introduced supplementary control loop in FPZPC. The injected supplementary stabilization signal is able to damp the system frequency so that to yield damped active power responses of all DG units. This is also consistent with the trend of dominant modes based on sensitivity analysis. Therefore, the proposed control scheme synthesizes the advantages of the conventional droop and supplementary control loop, providing fast response stabilization under disturbances.

Fig. 18 illustrates the impact of the communication delay on the frequency dynamic response to a step load increase of 300 kW. Fig. 18 suggests that the system frequency remains stable in the presence of large communication delay (200 ms) with the proposed frequency stability control scheme in FPZPC. Note that this is in line with the eigenvalue analysis shown in Fig. 15.

As previously described, the parameters of the proposed control scheme in FPZPC should be selected from the constraints of stability and the charging/discharging limits of the BESS. It can be seen from Fig. 17(c) that the active power of BESS increases to the peak of 280 kW during load disturbance, which exceeds the discharging limit P_{Bdmax}. Considering the maximum frequency deviation of the microgrid in steady state to be ±0.3 Hz (Zone A), f/P droop

TABLE IV
MEMS PARAMETERS SETTING

Parameter	Symbol	Setting	Unit
SoC Upper threshold	$SoC_{MEMSmax}$	95	%
SoC Low-threshold	$SoC_{MEMSmin}$	40	%
η Upper limit	η_H	70 ($N=1$); 60 ($N>1$)	%
η Low limit	η_L	30	%
Discharging power limit	$P_{Bd\max}$	210	kW
Charging power limit	$P_{Bc\max}$	–210	kW
Oscillation coefficient	K_{osc}	10	%
Regulating coefficient	K_{reg}	5	%
Sensitivity coefficient	K_{sen}	3	kW
Impact coefficient of WT start-up	k_{WT}	27	%
Penetration rate limit of start-up/shutdown WT	S_{pr1}, S_{pr2}	45, 30	%

TABLE V
MGCC PARAMETERS SETTING

Parameter	Symbol	Setting	Unit
SoC Upper threshold	$SoC_{MGCCmax}$	99	%
SoC Low-threshold	$SoC_{MGCCmin}$	20	%
Zone A	f_{AL}	49.7	Hz
	f_{AH}	50.3	Hz
Zone B-	f_{BL}	49.0	Hz
Zone B+	f_{BH}	51.0	Hz
Zone C-	f_{CL5}	45.0	Hz
Zone C+	f_{CH2}	55.0	Hz
Droop coefficient of f/P loop	K_{fP}	–250	kW/Hz
Droop coefficient of V/Q loop	K_{VQ}	–100	kVar/kV
Coefficient of the supplementary control loop	K_{scl}	0.1	kW.s^2
Filter cutoff frequency	ω_c	20π	rad/s

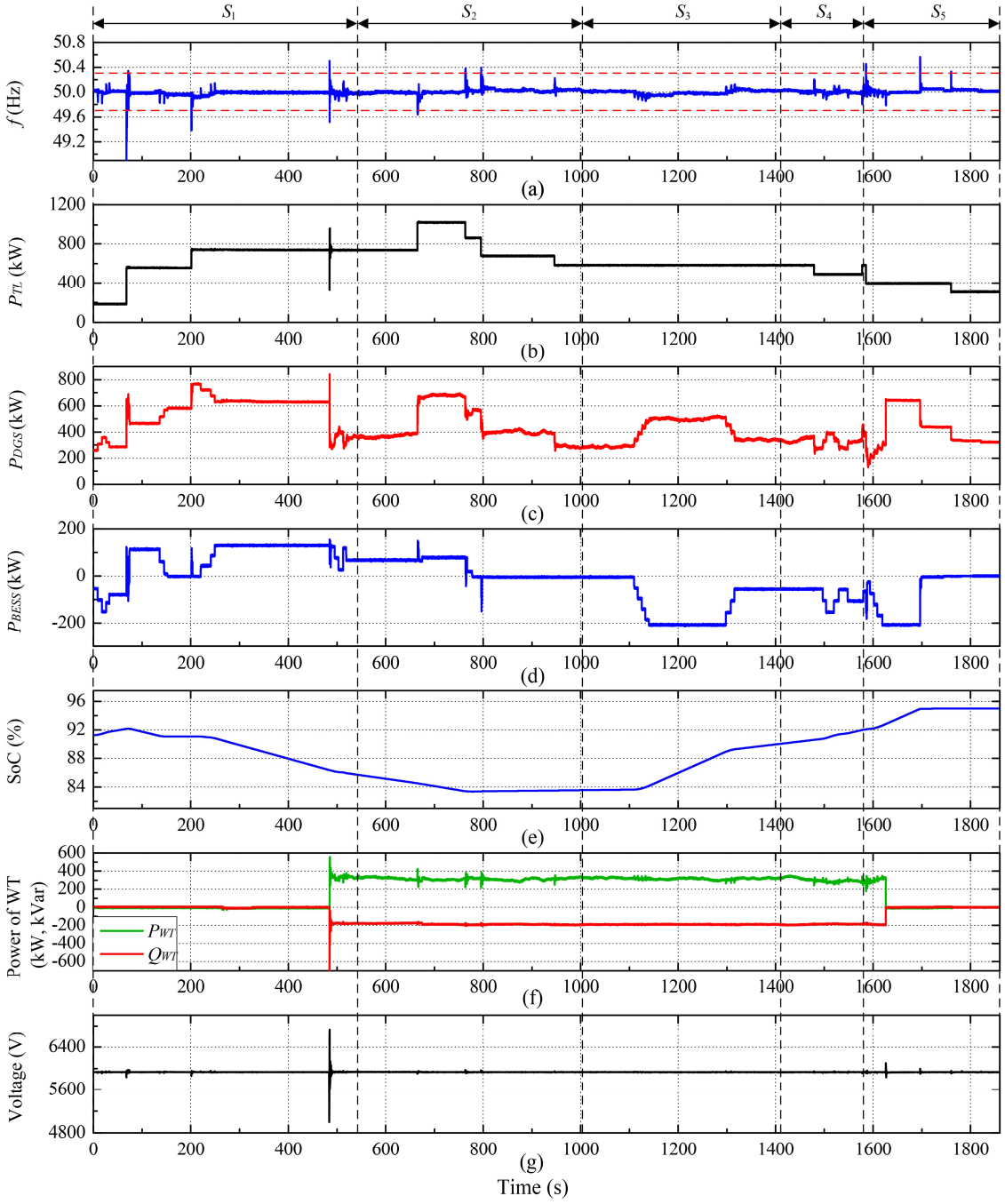

Fig. 20. System performances to continuous load variations with MGCC and MEMS. (a) Frequency. (b) Active power of the total load in microgrid. (c) Active power of DGS. (d) Active power of BESS. (e) SoC of BESS. (f) Active power (P_{WT}) and reactive power (Q_{WT}) of SCIG WT. (g) Voltage of BUS-2.

gain K_{fP} was selected a relatively smaller value (–250 kW/Hz). In regards to the selection of K_{scl} , although the sensitivity analysis in Fig. 11 suggests that K_{scl} can be higher to achieve better damping effect, the design of the supplementary control loop ($K_{scl} = 0.1\,\text{kW.s}^2$) is properly conservative. One of the main reason is that the charging/discharging limits of the BESS might be easily exceeded as the derivative term has a strong magnifying effect.

In addition to the parameters mentioned above, another main factor in the parameter selection of the proposed control strategy is the border of Zone B (f_{BL} , f_{BH}). As transient control measures, OFGT and UFLS of FEZPC have noticeable impact on the generators and prime movers in the microgrid because of the sudden change of the electrical and mechanical stress. Besides, frequency fluctuations are yielded even during normal OFGT or UFLS due to the low inertia characteristic of the microgrid, as shown in Fig. 21 of experimental test. In a practical microgrid design, in order to avoid the frequency falling into Zone C and triggering FEZPC, it is desirable to expand the frequency range of Zone B. However, on the one

hand, K_{fP} and K_{scl} are fixed by the designer to ensure desired transient response considering the charging/discharging limits of the BESS, thus the proposed control scheme in Zone B might limit to power saturation and become ineffective if the border is too large. On the other hand, the local frequency protection setting of all DG units and loads (e.g., the allowable frequency range of the SCIG WT is 47.5–52 Hz) must be within the frequency range of Zone C; otherwise, uncontrollable generator tripping and load shedding might lead to microgrid collapse. In this situation, the range of Zone B is chosen as a synthetic tradeoff taking into account the transient performance, power limit of BESS and the protection coordination of the microgrid.

B. *MEMS and MGCC Test Under Actual Conditions*

Multiple-time-scales hierarchical frequency stability control strategy is tested and verified in the Dongao Island MV microgrid under various actual conditions. Fig. 19 shows the main primary equipment and secondary equipment in the microgrid. The setting parameters of MEMS and MGCC are selected as presented in Tables IV and V respectively.

Fig. 20 shows the experimental test results of the MV microgrid performances during the process of continuous load variations when MEMS and MGCC are both enabled. The real scenarios of operation mode optimization in MEMS and rapid compensation control in MGCC are summarized as follows:

- Scenario S_1: The total load in the microgrid P_{TL} is rising from 188 kW to 752 kW gradually, and η exceeds the load rate upper limit η_H at $t = 202$ s, as shown in Fig. 20(b). Meanwhile, BESS increases the discharging power by ΔP_{MEMS1} as the spare capacity of the DGS ΔP_{sc} is not met to start up the WT. Then the command of WT start-up is issued by FSZPC scheme in MEMS as *Criterion 1* is satisfied. Afterwards, the SCIG WT connects to the microgrid smoothly at $t = 485$ s.
- Scenario S_2: The DGS is operating in normal range of load rate between η_L and η_H. Following continuous step load change, the power of the BESS is regulated by the FPZPC scheme in MGCC to stabilize the system frequency rapidly, as shown in Fig. 20(a).
- Scenario S_3: The charging power of the BESS is manually increased in remote control mode to speed up the charging process, as shown in Fig. 20(d). Thus, we can evaluate the system performance near the upper threshold of SoC of the BESS in scenario S_5.
- Scenario S_4: In order to be able to observe the power oscillation due to repetitively regulating the BESS nearby the load rate limit, K_{osc} is set to be zero in this case. As can be seen from Fig. 20(a) and (c), the system frequency and the output power of the DGS fluctuate up and down near η_L until K_{osc} is restored to nominal value.
- Scenario S_5: As η falls below η_L caused by a step load decrease of 200 kW, the charging power of the BESS grows gradually with ΔP_{MEMS2} until reaches the charging power limit $P_{Bc\max}$. Nevertheless, as shown in Fig. 20(e), the SoC of the BESS increases to 93.5% which almost reach the upper threshold 95%. Hence, the MEMS checks *Criterion 2* to shut down the DGS or the WT in advance. Resulting from *Criterion 2* is met, the SCIG WT is shut down according to the command issued by MEMS at $t = 1627$ s, as shown in Fig. 20(f).

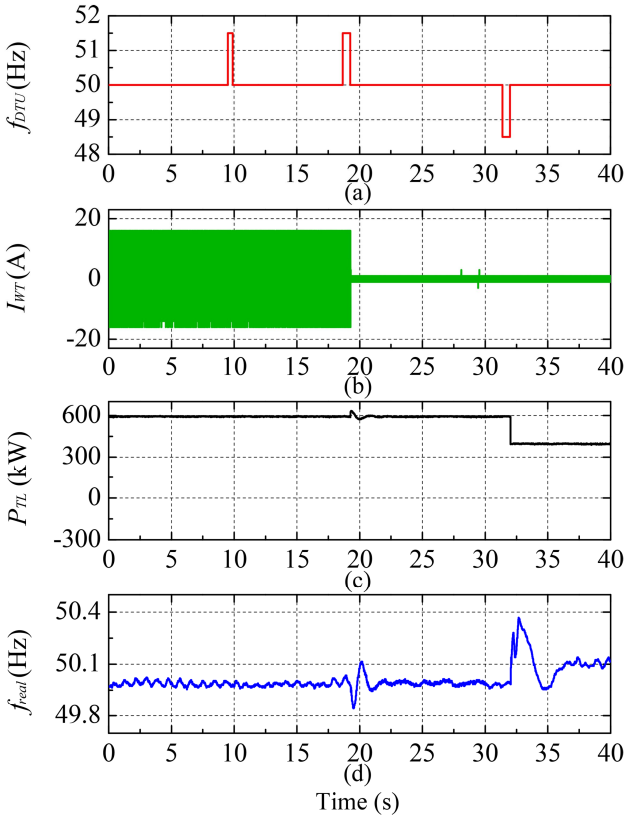

Fig. 21. Experimental test results of UFLS and OFGT functions in MGCC. (a) Simulated frequency signal fed in the DTU. (b) SCIG WT output current. (c) Active power of the total load. (d) Real frequency.

Consequently, it can be observed that the MEMS is capable of dealing with frequency fluctuations in long-time scale through optimization of microgrid operating mode, which is similar than the tertiary frequency control in interconnected power systems. Furthermore, there are ten times in which the frequency exceeds Zone A. Note that the frequency deviations caused by short-term large load demand can be suppressed by the MGCC effectively.

C. *Function Test of FEZPC in MGCC*

To test the validity of FEZPC scheme in MGCC under large disturbances (extreme conditions), simulated frequency signal generated using protection relay test system (PRTS) are fed in the DTU at BUS-1, which can be detected by the MGCC, as shown in Fig. 21(a). Fig. 21 shows the experimental test results of UFLS and OFGT functions in the MGCC. As can be seen from Fig. 21(a), there are three transient frequency pulses detected by the DTU, including 51.5 Hz last for 0.35 s at $t = 9.5$ s, 51.5 Hz last for 0.6 s at $t = 18.7$ s, and 48.5Hz last for 0.6 s at $t = 31.4$ s, respectively. However, only the second and

the third frequency pulse variations are valid and trigger OFGT at $t = 19.4$ s [see Fig. 21(b)] and UFLS at $t = 32.1$ s [see Fig. 21(c)], respectively, since the pulse-width in the first time is less than the setting delay time. It is shown that preventive control within emergency zone can be performed rapidly and correctly under the simulated extreme conditions.

VI. Conclusion

This paper introduces a hierarchical frequency control strategy to ensure power balance and frequency stability in multiple-time-scales for MV isolated microgrids. The proposed control strategy is realized with both dynamic and steady-state stability controllers based on different time scales. Dynamic stability control composed of preventive control in frequency precautionary and emergency zone is implemented by MGCC within 65 ms through GOOSE high-speed network. On the other hand, steady-state stability control which refers to the preventive control in frequency stable zone is executed by MEMS every 5 s through MMS supervisory network. By using the developed small-signal model of the MV microgrid, sensitivity analysis is conducted to analyze the dynamic stability margin of the microgrid and to identify the proper range of the main control parameters. Comprehensive simulated and experimental results in Dongao Island MV microgid are presented to verify the effectiveness of the proposed control strategy. It is shown that the coordination between dynamic stability control based on the millisecond level and steady-state stability control based on the second level is able to realize the stable and optimal operation of the MV microgrid in Dongao Island. This paper provides practical solution for the frequency control, with insight information about the configuration, modeling, analysis and operation of the MV isolated microgrid.

This study aims to solve the problem of the stable operation of the microgrid, especially concerning the frequency stability in the MV microgrid. The power quality improvement using distributed BESS in MV microgrid is subject to further research and will be considered in future studies of Dongao Island. Another important issue is that the application of proposed supplementary control scheme in other microgrids, e.g., microgrids with decentralized control architecture. In this application, the supplementary control scheme comprises the derivative terms of the local frequency and voltage. They can be included in the droop equations of (9) and (10) in [55] respectively, thus to improve the transient response of the microgrid. In order to evaluate the effectiveness of this extension further, modeling, analysis and testing of such microgrids are needed to conduct in future work.

References

[1] R. H. Lasseter, "Microgrids," in *Proc. IEEE Power Eng. Soc. Winter Meet.*, Jan. 2002, vol. 1, pp. 305–308.

[2] N. Hatziargyriou, H. Asano, R. Iravani, and C. Marnay, "Microgrids," *IEEE Power Energy Mag.*, vol. 5, no. 4, pp. 78–94, Jul. 2007.

[3] P. C. Loh, D. Li, Y. K. Chai, and F. Blaabjerg, "Autonomous operation of hybrid microgrid with AC and DC subgrids," *IEEE Trans. Power Electron.*, vol. 28, no. 5, pp. 2214–2223, May. 2013.

[4] J. M. Guerrero, J. C. Vasquez, J. Matas, L. G. de Vicuña, and M. Castilla, "Hierarchical control of droop-controlled AC and DC microgrids—A general approach toward standardization," *IEEE Trans. Ind. Electron.*, vol. 58, no. 1, pp. 158–172, Jan. 2011.

[5] J. A. Peas Lopes, C. L. Moreira, and A. G. Madureira, "Defining control strategies for microgrids islanded operation," *IEEE Trans. Power Syst.*, vol. 21, no. 2, pp. 916–924, May. 2006.

[6] E. Barklund, N. Pogaku, M. Prodanovic, C. Hernandez-Aramburo, and T. C. Green, "Energy management in autonomous microgrid using stability-constrained droop control of inverters," *IEEE Trans. Power Electron.*, vol. 23, no. 5, pp. 2346–2352, Sep. 2008.

[7] T. Dragicevic, J. M. Guerrero, J. C. Vasquez, and D. Skrlec, "Supervisory control of an adaptive-droop regulated DC microgrid with battery management capability," *IEEE Trans. Power Electron.*, vol. 29, no. 2, pp. 695–706, Feb. 2014.

[8] I. U. Nutkani, P. C. Loh, P. Wang, and F. Blaabjerg, "Cost-prioritized droop schemes for autonomous AC microgrids," *IEEE Trans. Power Electron.*, vol. 30, no. 2, pp. 1109–1119, Feb. 2015.

[9] J. M. Guerrero, M. Chandorkar, T. Lee, and P. C. Loh, "Advanced control architectures for intelligent microgrids—Part I: Decentralized and hierarchical control," *IEEE Trans. Ind. Electron.*, vol. 60, no. 4, pp. 1254–1262, Apr. 2013.

[10] Y. A.-R. I. Mohamed and E. F. El-Saadany, "Adaptive decentralized droop controller to preserve power sharing stability of paralleled inverters in distributed generation microgrids," *IEEE Trans. Power Electron.*, vol. 23, no. 6, pp. 2806–2816, Nov. 2008.

[11] J. He, Y. W. Li, J. M. Guerrero, F. Blaabjerg, and J. C. Vasquez, "An islanding microgrid power sharing approach using enhanced virtual impedance control scheme," *IEEE Trans. Power Electron.*, vol. 28, no. 11, pp. 5272–5282, Nov. 2013.

[12] M. Savaghebi, A. Jalilian, J. C. Vasquez, and J. M. Guerrero, "Secondary control scheme for voltage unbalance compensation in an islanded droop-controlled microgrid," *IEEE Trans. Smart Grid*, vol. 3, no. 2, pp. 797–807, Jun. 2012.

[13] A. Micallef, M. Apap, C. Spiteri-Staines, J. M. Guerrero, and J. C. Vasquez, "Reactive power sharing and voltage harmonic distortion compensation of droop controlled single phase islanded microgrids," *IEEE Trans. Smart Grid*, vol. 5, no. 3, pp. 1149–1158, May. 2014.

[14] E. Casagrande, W. L. Woon, H. H. Zeineldin, and D. Svetinovic, "A differential sequence component protection scheme for microgrids with inverter-based distributed generators," *IEEE Trans. Smart Grid*, vol. 5, no. 1, pp. 29–37, Jan. 2014.

[15] S. A. Saleh, "Signature-coordinated digital multirelay protection for microgrid systems," *IEEE Trans. Power Electron.*, vol. 29, no. 9, pp. 4614–4623, Sep. 2014.

[16] Microgrids Research Programme, Aalborg University: www.microgrids.et.aau.dk

[17] Y. Guan, J. C. Vasquez, J. M. Guerrero, Y. Wang, and W. Feng, "Frequency stability of hierarchically controlled hybrid photovoltaic-battery-hydropower microgrids," *IEEE Trans. Ind. Appl.*, to be published.

[18] B. Zhao, X. Zhang, and J. Chen, "Integrated microgrid laboratory system," *IEEE Trans. Power Syst.*, vol. 27, no. 4, pp. 2175–2185, Nov. 2012.

[19] B. Thomsen, J. M. Guerrero, and P. B. Thogersen, "Faroe islands wind-powered space heating microgrid using self-excited 220-kw induction generator," *IEEE Trans. Sustain. Energy*, vol. 5, no. 4, pp. 1361–1366, Oct. 2014.

[20] *Microgrid Symposiums*, [Online]. Available: http://microgrid-symposiums.org

[21] R. M. Kamel, A. Chaouachi, and K. Nagasaka, "Three control strategies to improve the microgrid transient dynamic response during isolated mode: A comparative study," *IEEE Trans. Ind. Electron.*, vol. 60, no. 4, pp. 1314–1322, Apr. 2013.

[22] J. Rocabert, A. Luna, F. Blaabjerg, and P. Rodríguez, "Control of power converters in AC microgrids," *IEEE Trans. Power Electron.*, vol. 27, no. 11, pp. 4734–4749, Nov. 2012.

[23] D. E. Olivares, A. Mehrizi-Sani, A. H. Etemadi, C. A. Canizares, R. Iravani, M. Kazerani, A. H. Hajimiragha, O. Gomis-Bellmunt, M. Saeedifard, R. Palma-Behnke, G. A. Jimenez-Estevez, and N. D. Hatziargyriou, "Trends in microgrid control," *IEEE Trans. Smart Grid*, vol. 5, no. 4, pp. 1905–1919, Jul. 2014.

[24] Y. Gu, W. Li, and X. He, "Frequency coordinating virtual impedance for autonomous power management of DC microgrid," *IEEE Trans. Power Electron.*, vol. 30, no. 4, pp. 2328–2337, Apr. 2015.

[25] K. D. Brabandere, B. Bolsens, J. V. D. Keybus, A. Woyte, J. Driesen, and R. Belmans, "A voltage and frequency droop control method for parallel inverters," *IEEE Trans. Power Electron.*, vol. 22, no. 4, pp. 1107–1115, Jul. 2007.
[26] A. Kahrobaeian and Y. A.-R. Ibrahim Mohamed, "Networked-based hybrid distributed power sharing and control for islanded microgrid systems," *IEEE Trans. Power Electron.*, vol. 30, no. 2, pp. 603–617, Feb. 2015.
[27] J. Hu, J. Zhu, D. G. Dorrell, and J. M. Guerrero, "Virtual flux droop method—A new control strategy of inverters in microgrids," *IEEE Trans. Power Electron.*, vol. 29, no. 9, pp. 4704–4711, Sep. 2014.
[28] H. Han, X. Hou, J. Yang, J. Wu, M. Su, and J. M. Guerrero, "Review of power sharing control strategies for islanding operation of AC microgrids," *IEEE Trans. Smart Grid*, to be published.
[29] J. He, Y. W. Li, and F. Blaabjerg, "An enhanced islanding microgrid reactive power, imbalance power, and harmonic power sharing scheme," *IEEE Trans. Power Electron.*, vol. 30, no. 6, pp. 3389–3401, Jun. 2015.
[30] N. Pogaku, M. Prodanovic, and T. C. Green, "Modeling, analysis and testing of autonomous operation of an inverter-based microgrid," *IEEE Trans. Power Electron.*, vol. 22, no. 2, pp. 613–625, Mar. 2007.
[31] A. Kahrobaeian and Y. A.-R. I. Mohamed, "Analysis and mitigation of low-frequency instabilities in autonomous medium-voltage converter-based microgrids with dynamic loads," *IEEE Trans. Ind. Electron.*, vol. 61, no. 4, pp. 1643–1658, Apr. 2014.
[32] N. Bottrell, M. Prodanovic, and T. C. Green, "Dynamic stability of a microgrid with an active load," *IEEE Trans. Power Electron.*, vol. 28, no. 11, pp. 5107–5119, Nov. 2013.
[33] Q. Shafiee, J. M. Guerrero, and J. C. Vasquez, "Distributed secondary control for islanded microgrids—A novel approach," *IEEE Trans. Power Electron.*, vol. 29, no. 2, pp. 1018–1031, Feb. 2014.
[34] Q. Shafiee, C. Stefanovic, T. Dragicevic, P. Popovski, J. C. Vasquez, and J. M. Guerrero, "Robust networked control scheme for distributed secondary control of islanded microgrids," *IEEE Trans. Ind. Electron.*, vol. 61, no. 10, pp. 5363–5374, Oct. 2014.
[35] J. W. Simpson-Porco, Q. Shafiee, F. Dorfler, J. C. Vasquez, J. M. Guerrero, and F. Bullo, "Secondary frequency and voltage control of islanded microgrids via distributed averaging," *IEEE Trans. Ind. Electron.*, to be published.
[36] J. G. de Matos, F. S. F. e Silva, and L. A. d. S. Ribeiro, "Power control in AC isolated microgrids with renewable energy sources and energy storage systems," *IEEE Trans. Ind. Electron.*, vol. 62, no. 6, pp. 3490–3498, Jun. 2015.
[37] D. Wu, F. Tang, T. Dragicevic, J. C. Vasquez, and J. M. Guerrero, "A control architecture to coordinate renewable energy sources and energy storage systems in islanded microgrids," *IEEE Trans. Smart Grid*, vol. 6, no. 3, pp. 1156–1166, May. 2015.
[38] X. Tang, W. Deng, and Z. Qi, "Investigation of the dynamic stability of microgrid," *IEEE Trans. Power Syst.*, vol. 29, no. 2, pp. 698–706, Mar. 2014.
[39] J.-Y. Kim, J.-H. Jeon, S.-K. Kim, C. Cho, J.-H. Park, H.-M. Kim, and K.-Y. Nam, "Cooperative control strategy of energy storage system and microsources for stabilizing the microgrid during islanded operation," *IEEE Trans. Power Electron.*, vol. 25, no. 12, pp. 3037–3048, Dec. 2010.
[40] D. E. Olivares, C. A. Cañizares, and M. Kazerani, "A centralized energy management system for isolated microgrids," *IEEE Trans. Smart Grid*, vol. 5, no. 4, pp. 1864–1875, Jul. 2014.
[41] J. Pahasa and I. Ngamroo, "PHEVs bidirectional charging/discharging and SoC control for microgrid frequency stabilization using multiple MPC," *IEEE Trans. Smart Grid*, vol. 6, no. 2, pp. 526–533, Mar. 2015.
[42] T. Logenthiran, D. Srinivasan, A. M. Khambadkone, and H. N. Aung, "Multiagent system for real-time operation of a microgrid in real-time digital simulator," *IEEE Trans. Smart Grid*, vol. 3, no. 2, pp. 925–933, Jun. 2012.
[43] H. S. V. S. Kumar Nunna and S. Doolla, "Multiagent-based distributed-energy-resource management for intelligent microgrids," *IEEE Trans. Ind. Electron.*, vol. 60, no. 4, pp. 1678–1687, Apr. 2013.
[44] "IEEE recommended practice for monitoring electric power quality," *IEEE Std 1159-2009 Revis. IEEE Std 1159-1995*, pp. c1–81, Jun. 2009.
[45] G. Manassero, E. L. Pellini, E. C. Senger, and R. M. Nakagomi, "IEC61850–based systems—functional testing and interoperability issues," *IEEE Trans. Ind. Inform.*, vol. 9, no. 3, pp. 1436–1444, Aug. 2013.
[46] H. Wu, K. S. Tsakalis, and G. T. Heydt, "Evaluation of time delay effects to wide-area power system stabilizer design," *IEEE Trans. Power Syst.*, vol. 19, no. 4, pp. 1935–1941, Nov. 2004.
[47] P. Kundur, *Power System Stability and Control*. New York, NY, USA: EPRI/McGraw-Hill, 1994.
[48] P. Krause, S. Sudhoff, and O. Wasynczuk, *Analysis of Electric Machinery and Drive Systems*. Hoboken, NJ, USA: Wiley-IEEE Press, 2002.
[49] "Dynamic models for fossil fueled steam units in power system studies," *IEEE Trans. Power Syst.*, vol. 6, no. 2, pp. 753–761, May. 1991.
[50] "IEEE recommended practice for excitation system models for power system stability studies," *IEEE Std 4215-2005 Revis. IEEE Std 4215-1992*, pp. 0_1–85, 2006.
[51] A. Tabesh and R. Iravani, "Small-signal dynamic model and analysis of a fixed-speed wind farm—a frequency response approach," *IEEE Trans. Power Deliv.*, vol. 21, no. 2, pp. 778–787, Apr. 2006.
[52] S. S. Choi and R. Larkin, "Performance of an autonomous diesel-wind turbine power system," *Electr. Power Syst. Res.*, vol. 33, no. 2, pp. 87–99, May 1995.
[53] R. Jayashri and R. P. Kumudini Devi, "Effect of tuned unified power flow controller to mitigate the rotor speed instability of fixed-speed wind turbines," *Renew. Energy*, vol. 34, no. 3, pp. 591–596, Mar. 2009.
[54] F. Milano and M. Anghel, "Impact of time delays on power system stability," *IEEE Trans. Circuits Syst. Regul. Pap.*, vol. 59, no. 4, pp. 889–900, Apr. 2012.
[55] J. M. Guerrero, J. C. Vasquez, J. Matas, M. Castilla, and L. G. de Vicuna, "Control Strategy for Flexible Microgrid Based on Parallel Line-Interactive UPS Systems," *IEEE Trans. Ind. Electron.*, vol. 56, no. 3, pp. 726–736, Mar. 2009.

Zhuoli Zhao (S'15) received his B.S. degree from South China University of Technology, Guangzhou, China, in 2010, where he is currently working towards the Ph.D. degree in electrical engineering in the National-Local Joint Engineering Laboratory for Wind Power Control and Integration Technology.

He is a Member of the Control and Power Research Group, Department of Electrical and Electronic Engineering, Imperial College London, London, U.K.. His research interests include microgrid stability and control, smart grids, and distributed generation systems.

Ping Yang (M'11) received her M.S. and Ph.D. degree in control theory and engineering from South China University of Technology, Guangzhou, China, in 1994 and 1998, respectively.

Currently, she is a Professor with the School of Electric Power at South China University of Technology. She is also the Director of National-Local Joint Engineering Laboratory for Wind Power Control and Integration Technology, and Key Laboratory of Clean Energy Technology of Guangdong Province. Her research interests include integration of renewable energy into power system, microgrid control and management, and prediction modeling for wind and solar power.

Josep M. Guerrero (S'01-M'04-SM'08-FM'15) received the B.S. degree in telecommunications engineering, the M.S. degree in electronics engineering, and the Ph.D. degree in power electronics from the Technical University of Catalonia, Barcelona, in 1997, 2000 and 2003, respectively. Since 2011, he has been a Full Professor with the Department of Energy Technology, Aalborg University, Denmark, where he is responsible for the Microgrid Research Program. From 2012 he is a guest Professor at the Chinese Academy of Science and the Nanjing University of Aeronautics and Astronautics; from 2014 he is

chair Professor in Shandong University; and from 2015 he is a distinguished guest Professor in Hunan University.

His research interests is oriented to different microgrid aspects, including power electronics, distributed energy-storage systems, hierarchical and cooperative control, energy management systems, and optimization of microgrids and islanded minigrids. Prof. Guerrero is an Associate Editor for the IEEE TRANSACTIONS ON POWER ELECTRONICS, the IEEE TRANSACTIONS ON INDUSTRIAL ELECTRONICS, and the IEEE Industrial Electronics Magazine, and an Editor for the IEEE TRANSACTIONS on SMART GRID and IEEE TRANSACTIONS on ENERGY CONVERSION. He has been Guest Editor of the IEEE TRANSACTIONS ON POWER ELECTRONICS Special Issues: Power Electronics for Wind Energy Conversion and Power Electronics for Microgrids; the IEEE TRANSACTIONS ON INDUSTRIAL ELECTRONICS Special Sections: Uninterruptible Power Supplies systems, Renewable Energy Systems, Distributed Generation and Microgrids, and Industrial Applications and Implementation Issues of the Kalman Filter; and the IEEE TRANSACTIONS on SMART GRID Special Issue on Smart DC Distribution Systems. He was the chair of the Renewable Energy Systems Technical Committee of the IEEE Industrial Electronics Society. In 2014 and 2015 he was awarded by Thomson Reuters as Highly Cited Researcher, and in 2015 he was elevated as IEEE Fellow for his contributions on “distributed power systems and microgrids.”

Zhirong Xu (S’15) received his B.S. degree in power systems from South China University of Technology, Guangzhou, China, in 2013, where he is currently working towards the Ph.D. degree in electrical engineering.

His research interests include microgrid energy management system and smart grids.

Timothy C. Green (M’89–SM’02) received the B.Sc. degree (first class Hons.) in electrical engineering from Imperial College, London, U.K., in 1986 and the Ph.D. degree in electrical engineering from Heriot-Watt University, Edinburgh, U.K., in 1990.

He was a Lecturer at Heriot Watt University until 1994 and is currently a Professor of Electrical Power Engineering at Imperial College London and the Deputy Head of the Control and Power Research Group. His research interests include using power electronics and control to enhance power quality and power delivery. This covers interfaces and controllers for distributed generation, micro-grids, active distribution networks, FACTS, and active power filters. He has an additional line of research in power MEMS and energy scavenging.

Prof. Green is a Chartered Engineer in the U.K. and a member of the Institution of Electrical Engineers.